Basal melt rates and ocean circulation under the Ryder Glacier ice tongue and their response to climate warming: a high resolution modelling study

Jonathan Wiskandt[1,2], Inga Monika Koszalka[1,2,3], and Johan Nilsson[1,2]

[1]Department of Meteorology, Stockholm University, Stockholm, Sweden
[2]Bolin Centre for Climate Research, Stockholm, Sweden
[3]Stockholm University Baltic Sea Centre, Stockholm, Sweden

Correspondence: Jonathan Wiskandt (jonathan.wiskandt@misu.su.se)

Abstract. The oceanic forcing of basal melt under floating ice shelves in Greenland and Antarctica is one of the major sources of uncertainty in climate ice sheet modelling. We use a high resolution, ~~non-hydrostatic~~ nonhydrostatic configuration of the Massachusetts Institute of Technology general circulation model (MITgcm) to investigate basal melt rates and melt driven circulation in the Sherard Osborn Fjord under the floating tongue of Ryder Glacier, northwestern Greenland. The control model configuration, based on the first ever observational survey by *Ryder 2019 Expedition*, yielded melt rates consistent with independent satellite estimates. A protocol of model sensitivity experiments quantified the response to oceanic thermal forcing due to warming Atlantic Water, and to the buoyancy input from the subglacial discharge of surface fresh water. We found that the average basal melt rates show a nonlinear response to oceanic forcing in the lower range of ocean temperatures, while the response becomes indistinguishable from linear for higher ocean temperatures, which unifies the results from previous modelling studies of other marine terminating glaciers. The melt rate response to subglacial discharge is sublinear, consistent with other studies. The melt rates and circulation below the ice tongue exhibit a spatial pattern that is determined by the ambient density stratification.

1 Introduction

Increasing ice mass losses from the Greenland and Antarctic Ice Sheets result from atmosphere-cryosphere-ocean interactions, which involve a range of processes including surface ice melt, internal ice dynamics and ocean-driven basal melt, wind, tides and sea ice, often coupled in a nonlinear way (Holland et al., 2008a; Straneo et al., 2012; Smith et al., 2020; Slater and Straneo, 2022). Fresh water flux from the melting ice sheets into the ocean leads to a global sea level rise and local impacts on coastal communities worldwide, and the observed acceleration of the ice sheet melt has been attributed to anthropogenic climate change (Fox-Kemper et al., 2021). A large community effort has thus been put forward to observe, quantify and understand the underlying processes and to develop representations (parameterizations) of the ice melt processes in climate models to improve the projections of future ice sheet mass loss and its impacts (Asay-Davis et al., 2017; Edwards et al., 2014; Cowton et al., 2015; Lazeroms et al., 2018; Sheperd and Nowicki, 2017; Nowicki and Seroussi, 2018; Pelle et al., 2019). This task is far from simple as the processes involved often feature small scales and complex geometries of both ~~,~~ ice and ocean ~~,~~ domains, and their interaction with the atmosphere.

The Greenland Ice Sheet (GrIS) holds about seven meters of sea level equivalent. It contributed 13.5 mm to the global sea level rise in the period 1992-2020, according to the most recent IPCC Report (AR6, Fox-Kemper et al., 2021). During this time there is evidence that the GrIS mass loss has accelerated in recent years (1995-2012) compared with the earlier period (Enderlin et al., 2014; Hill et al., 2018). The IPCC Report estimates a sixfold increase in mass loss rate in these last three decades from an average of 39 Gt yr^{-1} in the period 1992-1999 to 243 Gt yr^{-1} over the period 2010-2019 and projects the GrIS to likely contribute with 90-180 mm to sea level rise until 2100, while the Antarctic Ice Sheet contributes 30-340 mm (Fox-Kemper et al., 2021, SSP5-8.5). Ice mass loss from GrIS has a significant local fingerprint on several densely populated coastal regions worldwide (Rietbroek et al., 2016). Furthermore, freshwater input from the melting GrIS into the ocean has a potentially substantial (yet poorly quantified, and vividly debated) impacts on freshwater budget and dense water formation in the subpolar North Atlantic and hence on the strength and stability of the large scale thermohaline circulation (Rahmstorf et al., 2015; Boning et al., 2016; Luo et al., 2016; Rhein et al., 2018; Swingedouw et al., 2022).

The GrIS' marine terminating glaciers drain into long and narrow fjords that connect to the open ocean. The fjords are stratified with a deeper layer of warm and saline Atlantic Water (AW), overlaid by a colder and fresher Polar Water (PW) of Arctic origin (Straneo et al., 2012). The AW enters the Nordic Seas as an upper layer of the Norwegian Atlantic Current and undergoes deepening and cooling under its poleward pathway; upon reaching the Fram Strait the AW flow bifurcates into one branch recirculating cyclonically in the Nordic Seas and the Labrador Sea, and the other one taking a detour around the Arctic Ocean (Mauritzen et al., 2011; Koszalka et al., 2013; Rudels et al., 2015). The temperature and salinity properties of AW reaching the glacial fjords around Greenland varies thus regionally. The AW that reaches the northern coast of Greenland had circulated around the Arctic Ocean and is therefore the coldest variant of AW reaching the GrIS (Straneo et al., 2012). The exposure to thermal oceanic forcing (temperature difference between the ocean water and the ice) varies therefore regionally around Greenland in addition to local differences due to wind forcing, sea ice, the mesoscale circulation on the Greenland shelf, and the fjord geometry (Seale et al., 2011; Rignot et al., 2012; Enderlin and Howat, 2013; Sciascia et al., 2013; Straneo and Cenedese, 2015; Gelderloos et al., 2017; Schaffer et al., 2017; Jakobsson et al., 2020; Wood et al., 2021).

The interactions at the glacier-ocean interface leading to a freshwater flux from the GrIS is realized through three different processes: basal melting of the submerged glacial ice, subglacial discharge (SGD) of the surface melt water (the freshwater melting at the surface ice sheet due to atmospheric forcing and percolating down through the ice and toward the ice base) during the summer, and calving of icebergs at the ice front (Straneo and Cenedese, 2015). The respective importance of the processes is dependent on the time scale and the shape of the glacier terminus. The majority of glaciers in ~~the~~ southern Greenland terminate as grounded, vertical ice fronts (Hill et al., 2018). These so called tidewater glaciers feature fast rising buoyant plumes, because of the steepness of the ice ~~a~~ at the terminus (Rignot et al., 2010; Xu et al., 2012; Sciascia et al., 2013) and frequent iceberg discharge through calving. They are also subject to a relatively strong seasonal forcing due to the SGD (Sciascia et al., 2014; Straneo and Cenedese, 2015). A different type of ice-ocean interaction ~~considers the~~ occurs for ice shelves, i.e., the glaciers with ice tongues, found in the north of Greenland, including the Zachariae Isstrom (ZI), the

Nioghalvfjerdsfjorden, or 79°–North Glacier (79NG), the Ryder Glacier (RG) and the Petermann Glacier (PG). ~~Floating ice tongues~~ Under certain conditions, floating ice tongues can stabilize these glaciers by changing the stress balance and reducing the ice discharge across their grounding lines, an effect known as buttressing (Gudmundsson, 2013). On the other hand, due to the horizontal extent of the ice base, the area exposed to basal melting is much larger at ice shelves than it is at tidewater glaciers. The observed significant inter annual variability in the grounding line position of 79NG and the observed and modelled retreat of ZI and PG have been attributed to oceanic forcing (Wilson and F. Straneo, 2015; Mayer, 2018; Choi et al., 2017; Cai et al., 2017). However, due to remoteness and logistic difficulties with the measurements, the GrIS ice shelves and their fjord outlets are still sparsely observed with regards to the ocean-driven basal melt processes.

The basal melt beneath the glacier ice tongue acts as a buoyancy source, driving a rising buoyant plume that forms an outflow of glacially-modified water at its neutral density level. The entrainment into the plume drives an inflow of AW towards the ice base, establishing an estuarine circulation (Straneo and Cenedese, 2015). The basal melt processes beneath ice shelves have mostly been studied in the context of Antarctic ice shelves, and have been represented in terms of a basal melt parameterization combining the basic thermodynamic considerations, conservation laws and buoyant plume dynamics, and showing a good agreement with observations (e.g. Holland et al., 2008b; Jenkins, 1991; Jenkins et al., 2010; Jenkins, 2011; Reese et al., 2018). This has guided attempts to develop generalized versions applicable in climate models (Asay-Davis et al., 2016; Lazeroms et al., 2018; Pelle et al., 2019). However, questions remain regarding the applicability of this parameterization. One issue considers dependency of the melt on changing ambient ocean temperatures. In theory, the melt rate is linearly dependent on the ~~temperature~~ thermal forcing and the boundary layer velocity, which is also linearly dependent on the ~~temperature~~ thermal forcing through the buoyancy input from the melt ~~(e.g. Jenkins, 2011; Lazeroms et al., 2018)~~ (e.g. Holland et al., 2008b; Jenkins, 2011; Lazeroms et al., 2018); combining to a super linear dependency of melt on ~~temperature forcing. Several modelling studies~~ thermal forcing. Modelling studies considering melt rates at Greenland's tidewater glaciers with vertical ice fronts and exposed to relatively high oceanic forcing due to warm AW, however, simulate a dependency that is not significantly different from a linear one (Xu et al., 2012; Sciascia et al., 2013). Further questions consider the role of ambient ocean stratification, the ice-ocean interface geometry and the boundary layer (Holland et al., 2008b; Lazeroms et al., 2019; Bradley et al., 2021; Dansereau et al., 2013; Jordan et al., 2018). These questions are particularly relevant to the Greenland ice shelves, in addition to factors like fjord geometry, wind, sea ice, and seasonal variations of SGD. To our knowledge, there have only been few high-resolution ocean-circulation model studies on Greenlandic ice shelves: Cai et al. (2017) investigated the sensitivity of the PG basal melt and retreat to the oceanic thermal forcing and SGD.

The third largest remaining ice tongue in North Greenland belongs to the ~~Ryder Glacier (RG)~~ RG in North Greenland (54° W, 82° N, see Jakobsson et al. (2020), Figure 1). RG terminates in the Sherard Osborn Fjord (SOF) with an ice tongue extending about 20 km from the grounding line. In contrast to the other nearby glaciers with ice tongues, RG exhibited a varied retreat and advance pattern in recent decades (Hill et al., 2018; Wilson et al., 2017). Oceanographic surveys of SOF were completely lacking until the *Ryder 2019 Expedition* in August-September 2019 with the Swedish icebreaker Oden (Jakobsson et al., 2020). The expedition gathered a unique data set, including topographic data and hydrographic (temperature and salinity) profiles close to the ice-tongue front. The hydrographic profiles show a two-layer ~~like stratification~~ stratification typical of

Greenlandic fjords (Straneo et al., 2012) with a cold (about -1.5° C) and relatively fresh (salinity below 34 g kg^{-1}) surface layer (typical of Polar Surface Water, PSW) and a warm (0.2° C) and salty (34.7g kg^{-1}) layer of AW below 350 m. SOF is narrow ($\sim$ 10 km) rendering effects of the Earth's rotation negligible on the circulation, and a permanent sea-ice cover outside of SOF inhibits wind-driven water exchange between the fjord and the open ocean (Jakobsson et al., 2020). The estuarine exchange circulation in the SOF is thus driven primarily by the basal melt and the seasonal SGD flux. The weak dependence of the hydrography inside the fjord on the conditions outside distinguish RG-SOF system from the nearby glacier-fjord system at PG, and provides an interesting "laboratory" for observational and modelling studies of basal melt processes and melt-driven buoyant flows. Furthermore, observed and modelled increases of the AW temperature in the Nordic Seas and the Arctic Ocean (Münchow et al., 2011; Straneo and Heimbach, 2013; Wang et al., 2020) ~~rise~~ raise questions of the response of the RG to increasing oceanic thermal forcing; will it respond similarly or differently to the nearby PG?

This study presents results from a series of high-resolution ocean-circulation model simulations of basal melt and ocean ~~flow in a fjord with~~ circulation in a cavity below an ice tongue. The model geometry is idealised, but its qualitative features are selected to be representative for RG and SOF. Note that SOF has two sills ~~, which are not represented here. This is because the present focus is on flow and melt beneath the ice tongue, which are only indirectly affected by the sills : they primarily control the features of the~~ outside of the ice cavity; they are not considered in the model simulations presented here. The impact of the sills that control properties of AW reaching the ice ~~tongue~~cavity is a subject to a floow-up study. In control experiments, the model is initialized and, at the seaward end of the domain, restored to observations from the *Ryder 2019 Expedition* Jakobsson et al. (2020). We investigate the spatial variability of melt rates and melt driven circulation and perform sensitivity experiments to oceanic thermal forcing and SGD. In Section 2, we describe the model control configuration and the sensitivity experiments. Section 3 presents model results from the summer and a winter control simulation and the sensitivity experiments. In Section 4, we discuss implications of the results for the future evolution of the RG and include general considerations regarding the basal melt dependence on oceanic thermal forcing and SGD.

2 The model

We use the MITgcm (http://mitgcm.org) that solves the Boussinesq form of the Navier–Stokes equations as a ~~finite-difference~~ finite-volume discretization rendered on a horizontal Arakawa C-grid, and with vertical z-levels employing partial cells (Marshall et al., 1997; Adcroft et al., 2004). The model has been used previously to study the circulation in Greenland fjords with ~~tide water~~ tidewater glaciers (e.g. Xu et al., 2012; Millgate et al., 2013; Sciascia et al., 2013, 2014; Carroll et al., 2015; Jordan et al., 2018) and the ice shelf-ocean interactions for Greenland and Antarctic ice shelves (e.g. Dansereau et al., 2013; Cai et al., 2017).

In our study, we consider a high-resolution, idealized, nonhydrostatic setup with a rigid lid based on the survey of Jakobsson et al. (2020). The width of the inner fjord (ca. 9 km) is comparable to the first Rossby radius of deformation (7-10 km) which makes the across-fjord changes negligible compared to the variability along fjord (south-north) axis. Idealized three-dimensional simulations of the circulation in a SOF-like fjord with the local Coriolis parameter value confirm this notion

Table 1. Dimensional parameters used in the model simulations.

Name	**Symbol**	**Value**	**[Unit]**
Drag coefficient	c_D	1.5×10^{-3}	
Specific heat capacity Ice	$c_{p,i}$	2000	[J K^{-1} kg^{-1}]
Specific heat capacity water	$c_{p,w}$	3994	[J K^{-1} kg^{-1}]
Latent heat of fusion of ice	L_i	3.34×10^{5}	[J kg^{-1}]
Reference Salinity	S_0	35	[g kg^{-1}]
Reference Temperature	T_0	0	[$^\circ$ C]
thermal expansion Coefficient	α	0.4×10^{-4}	[$^\circ$ C^{-1}]
saline contraction Coefficient	β	8×10^{-4}	[PSU^{-1}]
thermal/saline exchange coefficient	$\gamma_{T,S}$		[m s^{-1}]
thermal conductivity of ice	κ_i	1.54×10^{-6}	[m^2 s^{-2}]
horizontal diffusivity in water (heat & salt)	κ_H	2.5×10^{-1}	[m^2 s^{-2}]
vertical diffusivity in water (heat & salt)	κ_V	2×10^{-5}	[m^2 s^{-2}]
Salinity coefficient of freezing temperature	λ_1	-5.75×10^{-2}	[$^\circ$ C psu^{-1}]
Constant coefficient of freezing temperature	λ_2	9.01×10^{-2}	[$^\circ$ C]
Pressure coefficient of freezing temperature	λ_3	-7.61×10^{-8}	[$^\circ$ C $Pa^{-}1$]
reference Density	ρ_0	999.8	[kg m^{-3}]
horizontal viscosity	ν_h	2.5×10^{-1}	[m^2 s^{-2}]
vertical viscosity	ν_v	1×10^{-3}	[m^2 s^{-2}]

(Yin, 2020). The rotational effects are thus neglected henceforth and the configuration is rendered two-dimensional (along fjord, vertical directions). Even at the neighbouring PG, terminating in a wider fjord of 20 km width, some previous studies used 2D configurations, neglecting rotational effects (Cai et al., 2017). On the other hand, Millgate et al. (2013) used a 3D setup and introduced variations in the ice bathymetry (channels) in the across-fjord direction and found rotational effects on the circulation under PG. Unlike at PG, the SOF at RG is much narrower and we do not have information about the spatial variations of the ice base so we keep the 2D setup. The model parameters are listed in Table 1.

The domain's dimensions and geometry are shown in figure 1a and b. We focus on the circulation in the ice shelf cavity, i.e., the first 30 km of the SOF with a horizontal grid spacing of $dx = 10$ m along the fjord axis. The model width in the across-fjord direction is one grid cell of size $dy = 10$ m. The domain is 1,000 m deep divided in 300 equally-spaced vertical levels ($dz = 3,33$ m). The first 20 km of the domain are covered by a floating ice shelf representing the RGs ice tongue. The ice tongue terminates in a 50 m deep front at $x = 20$ km. To represent the observations, the ice base is set to be a constant linear slope of s = 0.045, which is equivalent to an angle of $\phi = 0.045^\circ$, connecting the grounding line and the lowest point of the calving front (Fig. 1a). ~~The grounding line is set to~~ In the absence of detailed data about the ice and sea floor topography at the

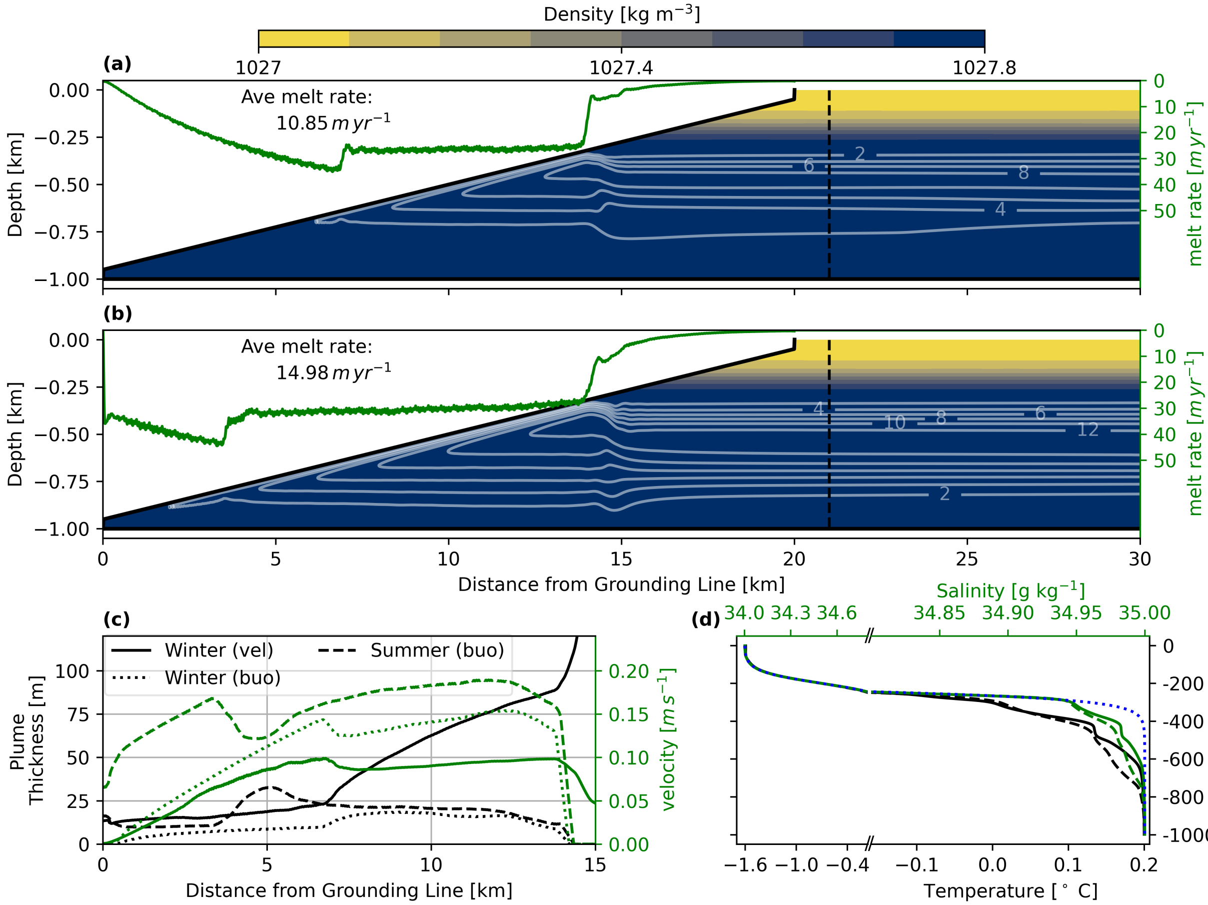

Figure 1. a) The stream function (white contours in m^2 s^{-1}) of the steady circulation superimposed on the density (σ, colors) and the melt rate (green line, right axis) along the ice ocean interface (black line) for *control_win*. The black dashed line indicates the location of profiles shown in figure 3 and 7; b) same as in a) but for *control_sum*; c) The plume thickness (black) calculated based on a combined velocity and buoyancy criterion ("buo") for summer (dashed) and winter (~~solid~~dotted) control simulation and for winter based on only velocity ("vel", solid); and the vertically averaged plume velocity (green)~~for summer (dashed) and winter (solid) control simulations~~. d) Initial and open ocean boundary condition profiles of salinity and temperature (showing as one blue dotted line for the chosen axes limits) and the steady state temperature (black) and salinity (green) profiles of the summer (dashed) and winter (solid) control simulations at $x = 21$ km.

grounding line we chose to keep a vertical wall below the lowest point of the ice shelf of 50 m ~~above the ocean floor to avoid instability issues~~ including a 20 m vertical SGD region (970 m to 950 m; see sect. 2.2) to leave room for inflowing AW and to avoid generation of strong property gradients at the corner ~~and leave a space for the plume to develop (Burchard et al., 2022)~~ of the domain. The bottom of the domain is flat. A quadratic drag is applied at the bottom of the domain and the ice.

All experiments are started from rest, initialized with horizontally uniform salinity (S) and temperature (T) profiles. In the control simulations these approximate the hydrographic profiles taken glacier ward of the inner sill just in front of the ice front (Station 16, 17 from figure 1 in Jakobsson et al. (2020)). ~~We set up a winter control simulation (*control_win*) without any subglacial discharge and a summer control simulation with subglacial discharge (*control_sum*).~~ For simplicity and because the nonlinear effects are small in the range of S-T values we are considering a linear equation of state for the density ρ:

$$\rho = \rho_0\left[1 - \alpha(T - T_0) + \beta(S - S_0)\right], \tag{1}$$

with parameters listed in Table 1. Sub grid scale processes are parameterized using a Laplacian eddy diffusion of temperature, salinity, and momentum with constant coefficients as in the MITgcm fjord simulation of comparable resolution by Sciascia et al. (2013). ~~At the model resolution, the mixing processes are dominated by turbulence, so~~ In the horizontal dimension we apply equal values of diffusion coefficients for ~~all variables (~~temperature, salinity and momentum (horizontal Prandtl number of unity) while in the vertical the viscosity is higher than tracer diffusivity to ensure numerical stability (Table 1). The MITgm applies the semi-implicit pressure method for nonhydrostatic equations with a rigid-lid, variables co-located in time and with Adams-Bashforth time-stepping. The advective operator for momentum is second order accurate in space. We apply a third order direct space-time tracer advection scheme with flux limiter due to Sweby (https://mitgcm.readthedocs.io/en/latest/index.html, sect. 2.17).

The northern ~~boarder~~ border of the fjord (at $x = 32$ km) is the only open boundary. The outflow is balanced at the boundary yielding a net zero cross boundary flow. Temperature and salinity are restored to the initial conditions in a 2 km wide restoring zone with a restoring timescale of one day at the innermost grid point ($x = 30$ km) and one hour at the outermost point ($x = 32$ km). An experiment conducted in a horizontally extended domain (not shown here) shows, that the boundary is sufficiently far away from the ice to have negligible effects on the evolution of the circulation underneath the ice tongue. We set up a winter control simulation (*control_win*) without any SGD and a summer control simulation with SGD (*control_sum*, see Section 2.2).

2.1 Basal melt parameterization

To parameterize the basal melt processes at the RG's ice shelf, we use the SHELFICE package[1] (Losch, 2008) applying ice ocean interactions in an interface mixed layer, defined as the uppermost grid cell adjacent to the ice ocean interface ~~(Dansereau et al., 2013; Jordan et al., 2018)~~(Dansereau et al., 2013; Cai et al., 2017; Jordan et al., 2018). Freezing and melting processes occur at the infinitesimal boundary layer at the interface and are paramaterized employing the three-equation formulation (Hellmer and Olbers, 1989; Holland and Jenkins, 1999):

$$T_b = \lambda_1 S_b + \lambda_2 + \lambda_3 P_b \tag{2}$$

$$c_{p,w}\rho_i\gamma_T(T_w - T_b) = -L_i q - \rho_i c_{p,i}\kappa_i \frac{(T_s - T_b)}{H_i} \tag{3}$$

$$\rho_i\gamma_S(S_w - S_b) = -S_b q \tag{4}$$

[1] https://mitgcm.readthedocs.io/en/latest/phys_pkgs/shelfice.html

The interface boundary layer temperature (T_b) is the in-situ freezing point temperature obtained from the boundary layer pressure and salinity (P_b and S_b respectively) using the linear equation of state (Eq. 1) where λ_j are constants. Equations 3 and 4, that describe heat and salt balances at the interface, respectively, are used to calculate S_b ~~. We~~ and q, where q is the upward freshwater flux (negative melt rate, in units of freshwater mass per time) and L_i is the latent heat of fusion. Upward heat flux implies basal melting (a downward freshwater flux), hence the minus sign (Losch, 2008). As in Cai et al. (2017) we assume a linear temperature profile in the ice and approximating the vertical temperature gradient in the ice as the difference between the ice surface ($T_S = -20°$ C) and interface (ice bottom) temperatures (~~T_i~~T_b) divided by the local ice thickness. Subscript w refer to the properties in the interface mixed layer. The values of parameters are listed in Table 1.

Exchange coefficients for salt and heat are calculated online (Holland and Jenkins, 1999) based on the along ice boundary layer velocity $\cancel{u^* = c_D\sqrt{u_{BL}^2 * w_{BL}^2}}$ $u^* = c_D\sqrt{u_{BL}^2 + w_{BL}^2}$, where c_D is the models drag coefficient and u_{BL} and w_{BL} are the local horizontal and vertical boundary layer averaged velocities. This yields:

$$\gamma_{T,S} = \frac{u^*}{\Gamma_{Turb} + \Gamma_{Mole}^{T,S}} \tag{5}$$

where Γ_{Turb} and $\Gamma_{Mole}^{T,S}$ are the turbulent and molecular exchange parameters defined as in Holland and Jenkins (1999) equations (15) and (16). The linear dependency of the exchange coefficient on the along-ice velocity u^* is expected to lead to a super-linear dependency of melt on the ~~temperature~~ thermal forcing, because u^* is approximated to ~~be~~ increase with increasing ~~temperature~~ thermal forcing through the change in buoyancy from enhanced melting (e.g. Jenkins, 1991; Holland et al., 2008a; Jenkins, 2011; Lazeroms et al., 2018).

Equations 2-4 are solved for boundary temperature and salinity and the melt rate q at every time step. The fresh water mass flux output (in ~~kilograms per square meter and second~~ [kg m^{-2} s$^{-1)}$]) is negative for melting, i.e., a downward mass input into the ocean. The temperature and salinity changes due to fresh water flux are implemented using virtual fluxes in the respective tendency equations. As the model employs partially filled cells, the parametrization uses a simple boundary layer averaging over vertical grid size dz. Velocities are averaged onto the tracer grid points. For further details about the ice shelf parametrization the interested reader is referred to Losch (2008).

2.2 Sensitivity experiments

We set up two sets of experiments, one without SGD and one with varying SGD. The goal of the first set of experiments is to elucidate on the dependency of basal melt on the oceanic thermal forcing. The second set is supposed to shed more light on how different SGD volumes influence the basal melt. Selected experiments are listed in table 2. For a complete list of experiments the interested reader is referred to the appendix tables A1 and A2.

Oceanic thermal forcing

First, we investigate a scenario of warming AW temperatures. To this end, we conduct a set of experiments with varying AW temperature (T_{AW}), while keeping PW temperature in the surface layer constant, applied as initial condition and boundary condition at the open ocean boundary. ~~We define a temperature forcing (TF= $T_{GL} - T_b$) where~~ The temperature profiles used

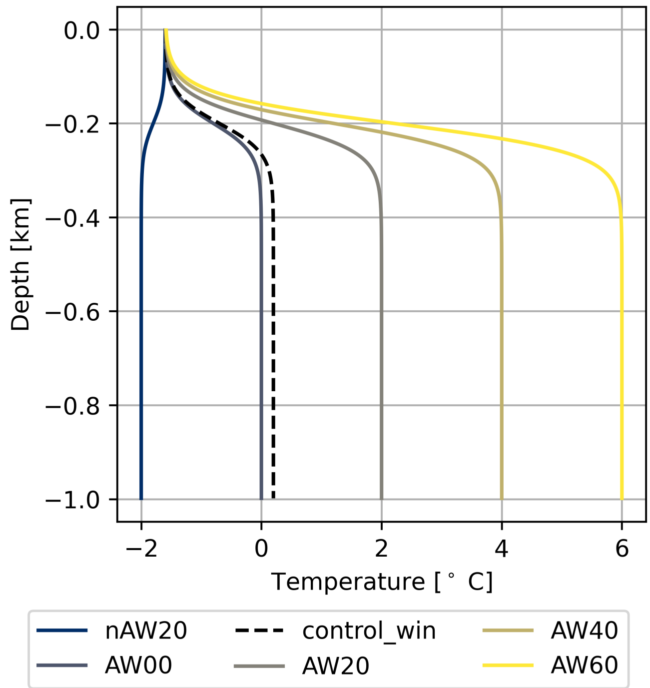

Figure 2. Initial and open ocean temperature profiles for a selected set of experiments with varying AW temperature.

to initialize and force the model are shown for a selected set of experiments (including warmest and coldest) in figure 2. A full list of experiments with their respective AW temperature is given in table A1. The salinity profile is the same for all experiments.

To quantify the response of the system in terms of melt rate and circulation changes to changing oceanic thermal forcing (by varying T_{AW}), we define an average temperature forcing TF= $T_{GL}(x_{GL}, z_{GL}) - T_f(x_{GL}, z_{GL})$ for each experiment, based on the time averaged fields when the model is in a statistical steady state (model days 61-100). T_{GL} is the time averaged water temperature at the grounding line ~~and T_b~~ (x_{GL}, z_{GL}) and T_f is the freezing point temperature evaluated at the ~~grounding line depth~~ same point using the local ~~salinity (S_b)and quantify the response of the system in terms of the melt rate and circulation changes to changing TF~~water salinity $S(x_{GL}, z_{GL})$. Note that the water at the grounding line is a slightly modified AW so T_{GL} is close to T_{AW}. Furthermore, T_f at the grounding line is essentially constant throughout all experiments at T_f = -2.68° C, hence we can approximate TF≈ T_{GL} +2.68° C (See tables 2, A1 and A2). We apply a wide range of AW temperatures to quantify the response of the melt rate and the resulting circulation to varying TF with more confidence.

Subglacial discharge

A second set of sensitivity experiments is conducted to investigate the influence of ~~subglacial discharge (SGD). Due to a lack of accurate estimates, the~~ SGD. In lieu of lacking information about the RG's subglacial channel geometry, we assume that the subglacial flux is dispensed evenly across the grounding line in a series of ice cavities 10 m (domain across-fjord width dy) in width and 20 m in height, analogous as in 2D setups of Sciascia et al. (2013) and Cai et al. (2017). The SGD volume fluxes are set ~~to fractions of~~ in relation to the integrated melt flux of the winter control simulation. ~~SGD is implemented by relaxing the values of temperature, salinity and horizontal velocity at the grounding line towards the local freezing point temperature, zero salinity and a discharge velocity calculated based on the discharge volume in the temperature and salinity tendency equations~~Direct observations at a nearby glacier (79NG) found that about 11% of the total fresh water leaving the cavity was from subglacial discharge (Schaffer et al., 2020). Therefore we set our lowest SGD volume (*SGD010*) to around 10% of total melt from *control_win*. Higher SGD is applied in multiples of *SGD010*. Using RCMs, Mankoff et al. (2020) and Slater et al. (2022) report estimated SGD of 357 $m^3\ s^{-1}$ = 11.26 $km^3\ yr^{-1}$ for a fjord width of around 11 km. Our highest SGD value, assuming a 10 km wide fjord, is around 40% of their value. For exact values of SGD volume applied in the presented simulations please refer to tables 2 and A2.

The subglacial flux is implemented as a source term in tracer and momentum conservation equations using MITgcm source and relaxation package RBCS (https://mitgcm.readthedocs.io/en/latest/phys_pkgs/rbcs.html). The discharge velocity is calculated as the ratio of the SGD volume flux to the area of the model cells where the SGD is applied. Note that the discharge velocity in MITgcm is applied in horizontal direction. The SGD fluxes for various experiments are presented in Table A2. These are rescaled from the dy = 10 m wide model domain to the estimated RG grounding line width of 10 km. We use a conservative third order direct space-time tracer advection scheme with flux limiter (Section 2) to avoid tracer extremes and the possibility of salinity going negative during the numerical integration when implementing SGD.

Steady state

All simulations were run for 100 days with a time step of ~~10*s* for the control runs andvarying time steps for sensitivity experiments~~ $2-10$ s depending on the strength of the oceanic thermal and/or SGD forcing to achieve model stability (Table 2). The statistically stationary equilibrium is reached after ca. 40 days for volume-averaged kinetic energy, circulation time scales and melt rates for all the runs (Figure B1 and B2), which is in line with an overturning time scale of 20-30 days. The integrated temperature change does not stabilize completely (Figure B1) for the two warmest runs but the deviations do not have significant effect on the other properties. For further analysis we use the last 40 days of simulation (model days ~~60-100~~61-100). The experiment setup details and key diagnostic values for a selected subset of experiments is given in Table 2. For the complete list of experiments we refer the reader to section A.

3 Results

3.1 Winter and summer control simulations

The steady state (model days 61-100) melt rates and circulation under the RG ice tongue for *control_win* and *control_sum* simulations are shown in figure 1a and b, respectively. Both cases exhibit an estuarine circulation typical of glacial fjords

Table 2. Setup parameters and diagnostics for selected experiments. From left to right: AW temperature, subglacial discharge volume in percent of *control_win* integrated melt volume, model time step, ~~temperature forcing~~TF, overturning time scale, averaged melt rate~~/ ice retreat~~, integrated melt flux ~~per unit width in transverse direction~~for a 10km wide fjord. For a complete account of all experiments see ~~section~~ Appendix A.

ExpName	T_{AW} [°C]	SGD Vol. [km^3 yr^{-1}]	dt [s]	TF [°C]	τ_o [days]	Ave. Melt [m yr^{-1}]	Melt Flux [km^3 yr^{-1}]
nAW20	-2.0	0.00	10	0.68	78	0.92	0.18
AW00	-0.0	0.00	10	2.68	27	15.28	3.06
control_win	0.2	0.00	10	2.87	27	17.36	3.47
AW20	2.0	0.00	10	4.67	23	37.43	7.49
AW40	4.0	0.00	5	6.66	22	61.34	12.27
AW60	6.0	0.00	5	8.65	22	83.91	16.78
control_sum	0.2	0.39	5	2.87	18	23.96	4.79
sgd020_AW02	0.2	0.78	5	2.87	15	26.67	5.34
sgd050_AW02	0.2	1.94	5	2.87	12	31.60	6.32
sgd100_AW02	0.2	3.88	3	2.86	10	36.67	7.34
sgd100_AW20	2.0	0.39	5	4.67	17	47.96	9.60
sgd010_AW40	4.0	0.39	5	6.65	16	76.59	15.33

(Straneo and Cenedese, 2015): the warm AW inflow in the lower layer supplies heat to the ice base forcing basal melting. The melt water input drives a buoyant plume, which rises into the base of the pycnocline (located at about 400 m depth) where it reaches its level of neutral buoyancy and forms a horizontal outflow jet towards the open boundary. The overturning time is estimated from the model domain volume (V_d) divided by the integrated AW volume transport at $x = 21$ km ($\tau_O = \frac{V_d}{\int\int u_{AW}(z)\,dz dy}$) and yields 27 days (winter) and 18 days (summer, Table 2).

Restoring to the initial stratification at the open boundary results in a continuous oceanic heat transport toward the ice base sustaining the basal melt (Eqs. (2) - (4)). The steady state melt rates along the ice base are shown in figure 1a and b, and the average values are shown in table 2. Both, winter and summer control simulations, exhibit ~~negative~~ positive average melt rates, corresponding to equivalent ice thickness loss and potential glacier retreat. In *control_win*, the average melt rate is 17.36 m yr^{-1} but the melt rates are variable along the ice base (Figure 1a and b): rising from zero at the GL to a maximum of 35.08 m yr^{-1} at about 7 km where they drop slightly to a value around 27 m yr^{-1} persisting until 14 km, and then dropping ~~to~~ towards zero. This spatial melt rate distribution is related to the buoyant plume properties (see below). The melt water flux integrated along the 20 km long ice shelf amounts to 3.47×10^5 m^2 yr^{-1} per unit width, or 2.95–3.47 km^3 yr^{-1} for the estimated glacier tongue width of 8.5–10 km. For the control summer simulation, the average basal melt increases to 23.96 m yr^{-1} (or 4.07–4.79 km^3 yr^{-1}), which is an increase of 38% compared to the winter control. The summer control shows a similar variability of

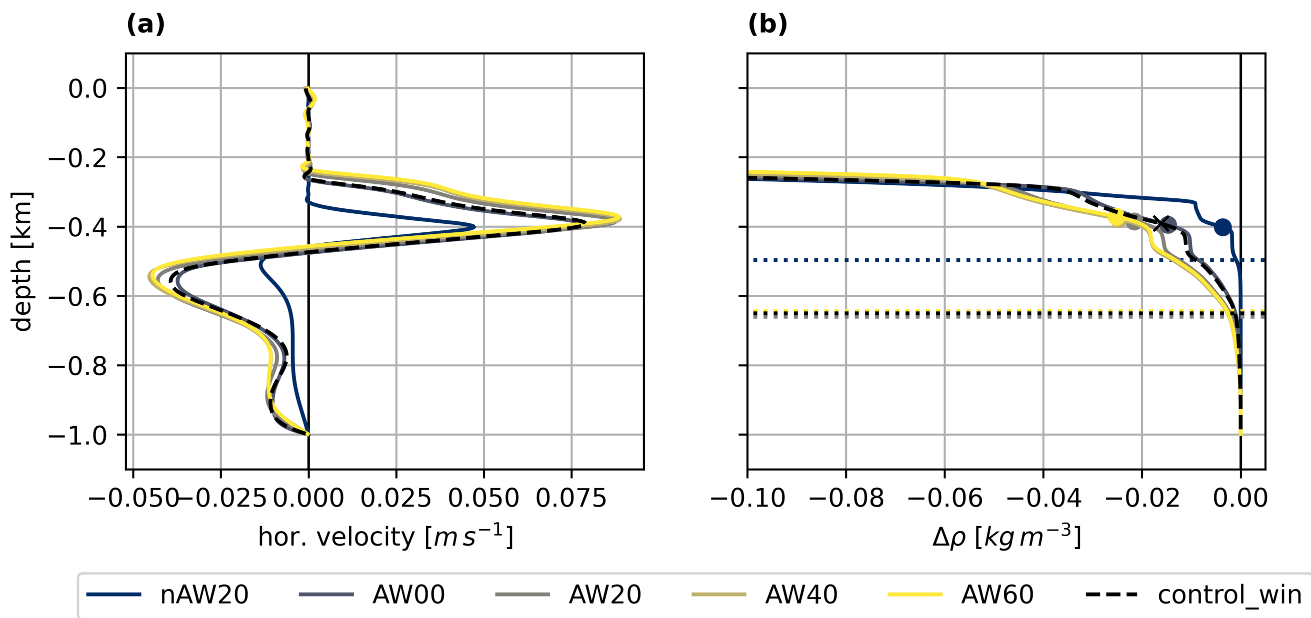

Figure 3. Profiles (solid lines) at 21 km from the *control_win* and selected ~~temperature~~ oceanic thermal forcing experiments of (a) horizontal velocity and (b) density change with respect to bottom density, $\Delta\rho = \rho(z) - \rho(z = 1km)$. Dots in (b) indicate the depth of maximum horizontal velocity. The dotted horizontal lines in (b) indicate the depth of maximum melt (corresponding to the plume's regime transition point depth).

melt rates along the ice base to the winter control but for the immediate buoyancy input at the GL, which leads to the melt rate maximum shifting the transition zone from 7 km to closer to the GL at 4 km where the maximum melt rate is 44.50 m yr^{-1}, and a subsequent drop to an approximately constant 30 m yr^{-1} persisting until 14 km, and then dropping ~~to~~ towards zero. This shift of transition zone (7 km in winter vs. 4 km in summer) collocates with a downward thickening of the ambient pycnocline (Figure 1d).

We will here describe the melt driven circulation for the winter simulation, and examine effects of changes of thermal forcing and SGD in the following sections. To characterize the buoyant plume, we define the plume as the region beneath the ice base where $u > 0$ (the flow is towards the open ocean). We tried alternative definitions of the plume based on the temperature and salinity difference compared to the ambient and prescribed stratification. These resulted in a narrower or wider plume over the distance between 7 and 14 km ~~.~~ depending on the value of temperatre and salinity used. For values closer to these of ambient stratification, the resulting plume was wider. As the difference encompasses the region of no horizontal flow outside the plume (by definition $u \leq 0$ here), this has no impact on the further calculations of e.g., plume transport~~and we decide to stick with the definition based on the horizontal velocity.~~

~~The~~ . Using a buoyancy criterion, i.e. temperature and salinity combined, and defining a threshold (75th percentile) results in a narrower and relatively well mixed plume, i.e. in characteristics more comparable to the plume of Jenkins (1991, 2011).

To quantify this, we show the plume thickness and averaged plume velocity ($u_p = \sqrt{u^2 + w^2}$) ~~are shown~~ in figure 1c. Clearly distinguishable are two different plume regimes during its ascent along the ice base, no matter the way of defining the plume: the accelerating plume and the thickening plume. ~~In the~~ When using the velocity criterion, in the accelerating plume regime close to the GL, the plume has a thickness of around 20 m, while the ~~average~~ vertically averaged plume velocity increases steadily to a maximum of 0.1 m s^{-1} at 7 km. In the thickening regime the velocity is around 0.095 m s^{-1} and the plume thickness increases from 20 m to 90 m between 7 km and 14 km. ~~This two-regime structure is evident in other plume properties (e.g., temperature, salinity and density; not shown) and is corresponding to the spatial variability in the melt rates described above.~~ The depth of the transition from accelerating to thickening plume is linked to the ambient stratification in the fjord (Figure 1d, see Section 3.2 and 3.3). The average plume thickness is around 40 m for all experiments.

Note however that the plume defined by velocity only is still stratified, so it is not fully equivalent to the ”well mixed plume” in the sense of Jenkins (2011)'s plume model. If we define the plume by adding a buoyancy criterion (only the 75th percentile of buoyancy values in the velocity plume), the plume is narrower with higher average velocities compared to the original definition based on velocity only (Figure 1c). Notably, the plume accelerates strongly in the first regime to a local maximum average velocity of 0.14 m s^{-1} and shows a significant decrease of velocity at the regime transition but subsequently starts again to accelerate in the second regime. The overall higher velocities using the buoyancy plume definition arise because the region of low velocities further away from the ice is not considered.

At 14 km, the plume velocity drops ~~to~~ towards zero (Figure 1c) which marks the location where the plume separates from the ice (Figure 1a,b) and forms a horizontal outflow jet towards the open boundary. The outflow layer is about 250 m thick (spanning 250–500 m depth) with a maximum velocity at 400 m (Figure 3a). The outflow forms a T-S transition layer between the AW and the PW, that was smoothed out in the idealized initial profiles (Figure 1d and 3b). This ~~transition is recognizable in~~ layer is characterized by a cooling and freshening compared to the initial profile, in line with what would be expected from glacially modified water. This glacially modified layer can also be found in the observations of (Jakobsson et al., 2020) (see their figure 2), lending confidence to the model results. The outflow at intermediate depth is balanced by an AW inflow in the bottom layer with a maximum velocity of -0.04 m s^{-1} just below 500 m and a secondary maximum close to the bottom (Figure 3a). The plume is not sufficiently buoyant to penetrate into the upper layer of PW which remains undisturbed.

3.2 Sensitivity to oceanic thermal forcing

We will first describe the results of the winter simulation without SGD for different temperature scenarios, before looking into the effect of the varying SGD (Sect. 3.3). We applied a wide range of AW temperatures to quantify the response of the melt rate and the resulting circulation to varying ~~TF~~ oceanic thermal forcing with more confidence~~. The response of the melt driven circulation to changing temperature forcing (TF)~~ , which is shown in figures 3 and 4. The structure of the circulation and the distribution of the plume properties is the same for all experiments, except of those with very low AW temperatures (TF$< 2°$ C, $T_{AW} < -1.0°$ C). The plume thickness and its velocity (Figure 4a and b), thus the volume transport, change only slightly in response to the increased melt for warmer experiments (Figure 4c). The increased melt water input freshens and cools the plume and the outflow, sharpening the density gradient at the base of the pycnocline in the outflow without changing its thickness

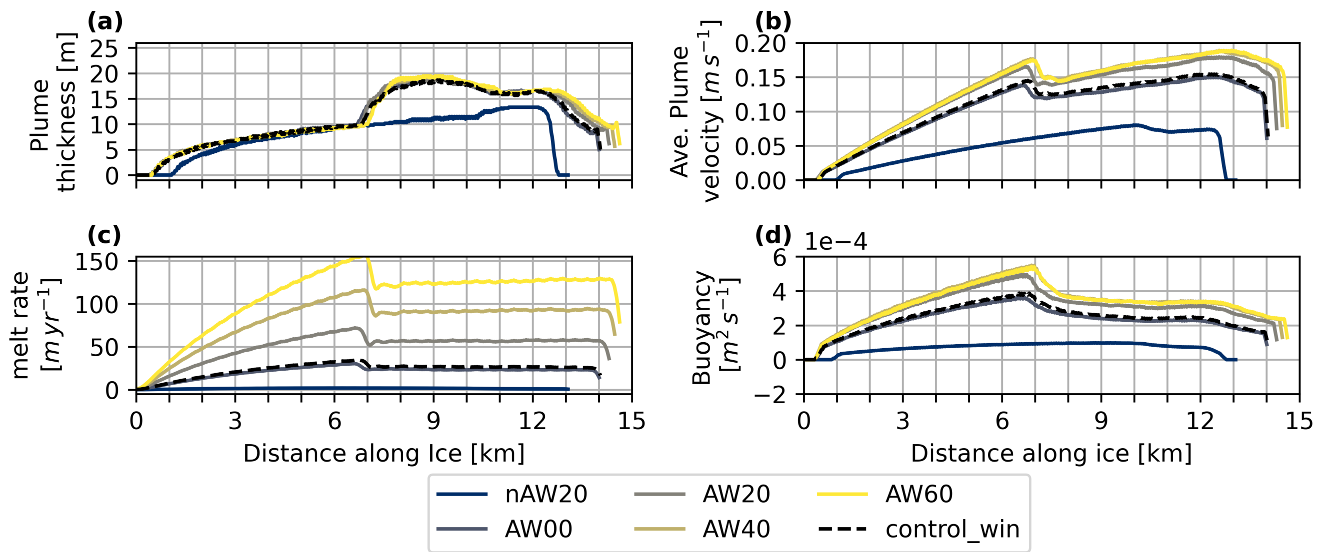

Figure 4. Plume properties for simulations with varying oceanic thermal forcing (AW temperatures) as a function of distance from the grounding line along the ice: (a) plume thickness, (b) averaged plume velocity, (c) melt rate and (d) Buoyancy (see text).

(Figure 3b). Figure 4d shows the buoyancy in the plume, estimated ~~as~~ from the density difference between the local plume density (ρ_p) and the ambient ocean density (ρ_a) at 21 km: ~~$b = (\rho_a(x = 21km, z) - \rho_p(x, z))\, g$~~ $b = \frac{\rho_a(x=21km,z) - \rho_p(x,z)}{\rho_0} g$. Because of the competing effect of freshening and cooling on the density, there is no effective change of buoyancy forcing with increasing TF. For the coldest experiments, i.e., weak oceanic thermal forcing, the melt rate is lower and the plume ~~does not develop the two-regime structure we see in warmer experiments~~shows the shift to the secondary regime only around 10 km (Figure 4a,b) at a depth of around 500 m (Figure 3b).

The horizontal dashed lines in figure 3b show the depth of maximum ~~melt rates corresponding to the plume transition between the accelerating and thickening~~ decrease of vertically averaged plume velocity before the detachment, which is also the depth at which the plume transitions from the accelerating to the thickening regime (Section 3.1)~~with respect to the ambient stratification~~. For all experiments the depth of the transition coincides with the base of the pycnocline marked by $\Delta\rho < 0$ (at about 620 m depth). This suggests that the spatial structure in the melt rates and the transition between the accelerating and thickening plume at 7 km is determined by the ambient stratification. The evolution of the vertically averaged plume buoyancy along the ice underpins this conclusion further, as the maximum buoyancy coincides with the point of regime transition for various TF experiments (Figure 4d).

Figure 5a shows the average melt rate for a wide range of ~~oceanic thermal forcing (TF)~~TF. We quantify the response to oceanic thermal forcing using regression analysis (e.g., Storch and Zwiers, 1984) and a resampling technique. A linear regression fit has high residuals for low TF values. We then construct sample subsets by successively excluding data points from cold experiments, starting with the coldest, and re-evaluate the linear fit. In doing so, we find the highest coefficient of

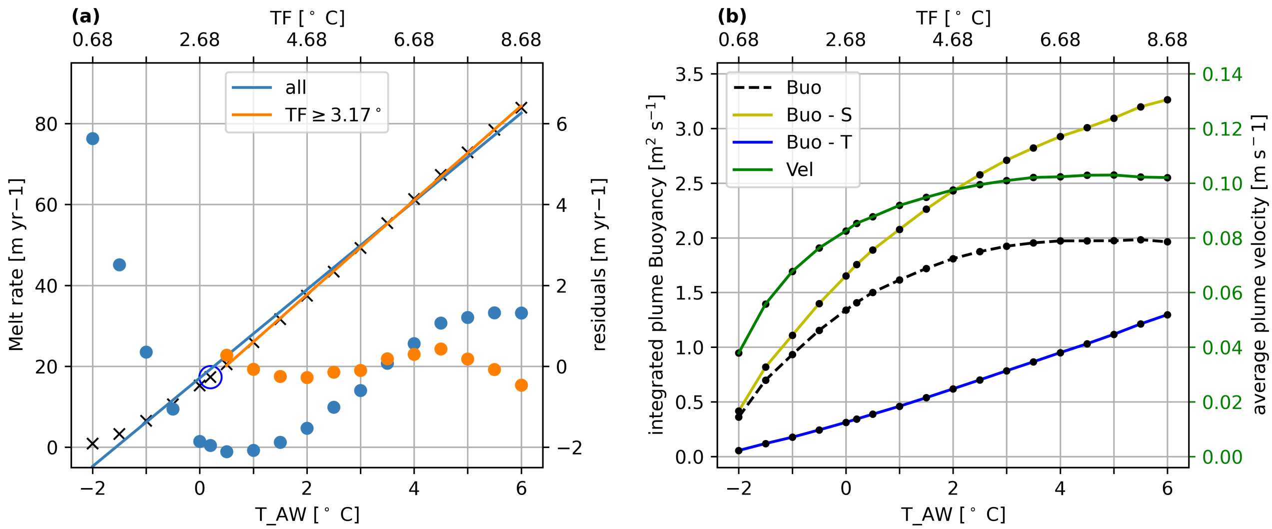

Figure 5. (a) The average melt (left ordinate axis) as a function of AW temperatures (T_{AW}; bottom abscissa) corresponding to ~~thermal~~ temperature forcing (TF; top abscissa) for winter experiments (without subglacial discharge). Superimposed are the linear fit for all experiments (blue line) and for intermediate to warm experiments only (orange line; see text). The corresponding residuals (right ordinate axis) are plotted with dots. *control_win* is marked with a blue circle. (b) The plume averaged buoyancy due to temperature (Buo-T; blue; absolute values of the negative function are shown), salinity (Buo-S; yellow) and the combined influence on density (Buo, black dashed).

determination (R^2) and the lowest root mean squared error of a linear fit for experiments with a temperature forcing ~~larger than the cut-off value 2.88 <TF$_c$ < 3.18° C (~~TF≥ 3.18° C (*AW05*, Figure 5). The adjusted linear fit has smaller residuals ~~across the whole TFrange~~ for all TF≥ 3.18° C (Figure 5a) implying a non-linear dependency of melt flux on TF for TF≤ 2.88° C (*control_win*) and a linear dependency for TF≥ 3.18° C (*AW05*). The fitted linear increase of melt per degree warming of AW is 11.69 m yr^{-1} K^{-1} or roughly two thirds of the modelled melt under winter conditions (17.36 m yr^{-1}) per degree warming.

The integrated cooling and freshening effect on the plume's buoyancy is summarized for all temperature sensitivity experiments in figure 5b. The buoyancy due to the plume temperature (Buo-T) and salinity (Buo-S) is calculated as the buoyancy in figure 4 but from the respective difference between temperature and salinity using the linear equation of state (Equation 1) and integrated vertically and horizontally over the plume. For higher temperature forcing (TF≥TF$_{\cancel{c}c}$ = 3.18° C, Table A1) the buoyancy is ~~not~~ no longer increasing linearly with TF. The effect of temperature and salinity start to balance one another and the total buoyancy becomes independent of temperature for experiments with ~~thermal~~ temperature forcing of TF> 6.18° C (*AW35*), resulting in a plateauing of average plume velocities (green in figure 5b). We elaborate on this in Section 4, *Response to oceanic thermal forcing*. This explains the very weak response of plume velocity to the oceanic thermal forcing at higher TF (~~Sect. 3.1~~Figure 4b). Consistently, the fjord overturning time scale decreases with TF for colder experiments (implying a faster overturning) but saturates around 22 − 23 days for the warmer simulations (Table 2 and A1).

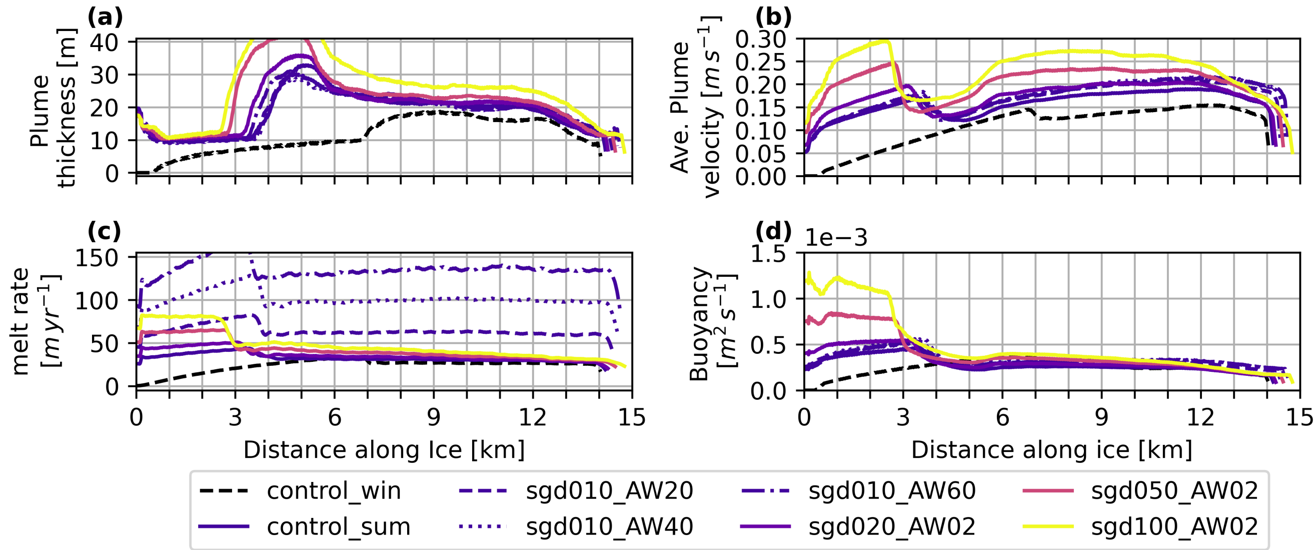

Figure 6. Same as Figure 4 but for different SGD volume fluxes and AW temperatures.

3.3 ~~Sensitivity to subglacial discharge~~

~~Subglacial discharge (SGD)~~

3.3 Sensitivity to subglacial discharge

SGD has a pronounced effect on the basal melt rates. The average melt rate for the *control_sum* simulations (where SGD is set to 10% of the average basal melt flux for the control winter; Table 2), is increased by 38% (from 17.36 m yr^{-1} to 23.96 m yr^{-1}, Table 2). For the experiment with the highest SGD (*sgd100_AW02* in table 2) the increase in melt is 111% (36.67 m yr^{-1}).

Not only does the total melt change, but so does the melt rate distribution along the ice base and the plume properties (Figure 6). The buoyancy input from SGD ~~lead~~ leads to high plume velocities at the GL resulting in higher melt rates there (Figure 6~~a-b~~b-c). While for all experiments the accelerating and thickening plume regime identified in *control_win* are distinguishable by thickness, velocity and melt (Figure 6a-c), the point of transition moves towards the GL. For *control_sum* ~~, *sgd010_AW20* and *sgd010_AW_40*~~ the transition point jumps more than 3 km closer to the GL (from 7 km in *control_win* to 3.5–4 km in *control_sum*). When increasing the discharge further, the migration of the point of transition towards the GL becomes less rapid (to 3–3.5 km for 20% discharge, to <3 km for 50% and 100% discharge). This does not immediately reflect in a thickening of the plume (Figure 6~~b~~a), which is only slightly increased compared to the *control_~~win~~sum*. Despite starting with already high velocities, the plume does accelerate further in the first regime, while the melt rate increases and the thickness stays constant,

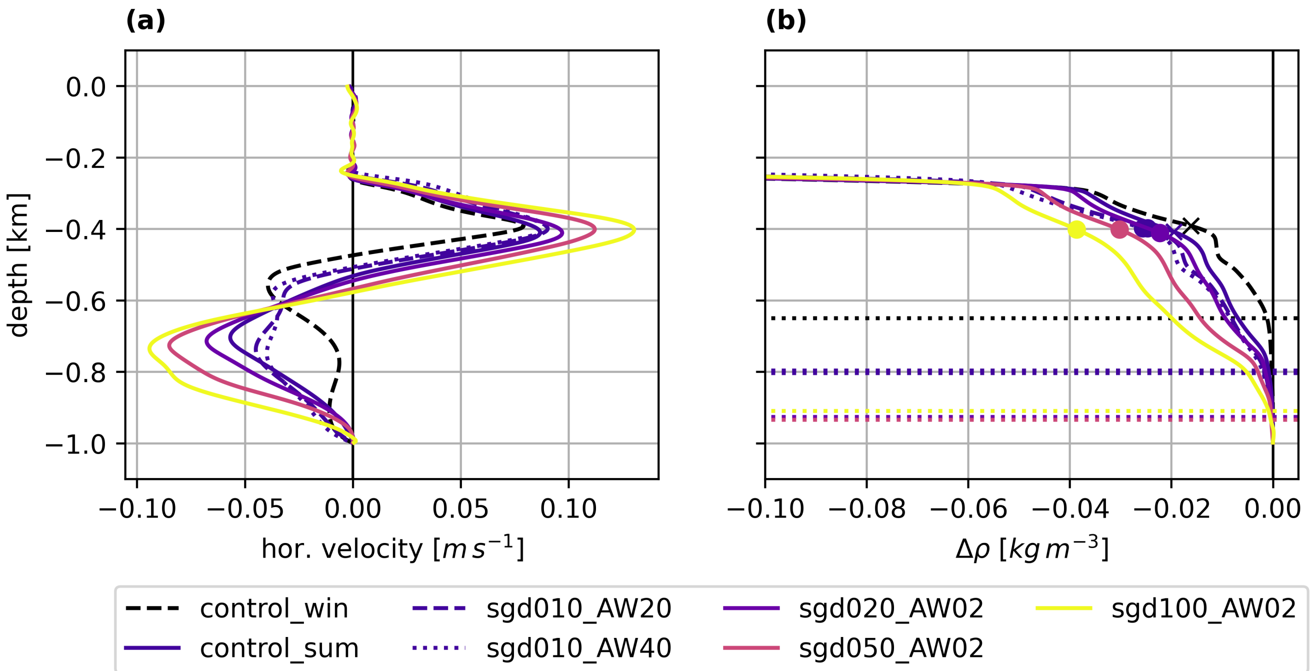

Figure 7. As Fig. 3 but for different SGD volume fluxes.

similar to the winter simulations. In the thickening regime, after a slow down of the plume, the velocities and melt rates become ~~virtually constant while the plume continues to thicken~~ almost constant (Figure 6).

The increased melt water input in simulations with SGD leads to a fresher, colder and faster outflow and a downward shift of the base of the pycnocline (Figure 7a-b), more pronounced for experiments with higher SGD. This downward shift of the base of the pycnocline to a depth of about 800 m is related to the spatial structure of the melt rates and the shift of transition zone between the accelerating and thickening plume regimes (Figure 6a-c and Figure 7b; horizontal dotted lines), consistent with findings in Sect. 3.2 (Figure 3). The distribution of the plume buoyancy along the ice base underpins this conclusion further, as the ~~maximum~~ sudden decrease in buoyancy coincides with the point of regime transition for all SGD experiments (Figure 6d).

The effect of oceanic thermal forcing (increasing TF) on simulations with ~~subglacial discharge~~ SGD is shown in figure ~~8.~~ 7. It leads to the following observations: ~~i) the~~

1. The functional response of the melt rate to TF found in the winter simulations (without SGD; Figure ~~5a~~4a) holds for the simulations with SGD (Figure 8a)~~, ii) there is stronger linear increase in~~. For the experiments conducted, the linear regression (dotted lines in figure 7a) fit with the simulated melt rates for TF≥3.18°C.

2. The linear increase of the melt rate ~~with TF for experiments with SGDas compared to the experiments without SGD(Figure 8a), iii) for experiments with~~ becomes stronger, for higher SGD; 14.02 m yr^{-1} K^{-1} for *SGD010*, 15.47 m yr^{-1} K^{-1} for *SGD020*, 17.68 m yr^{-1} K^{-1} for *SGD050*, 18.80 m yr^{-1} K^{-1} for *SGD070* and 20.17 m yr^{-1} K^{-1} for *SGD100*, compared

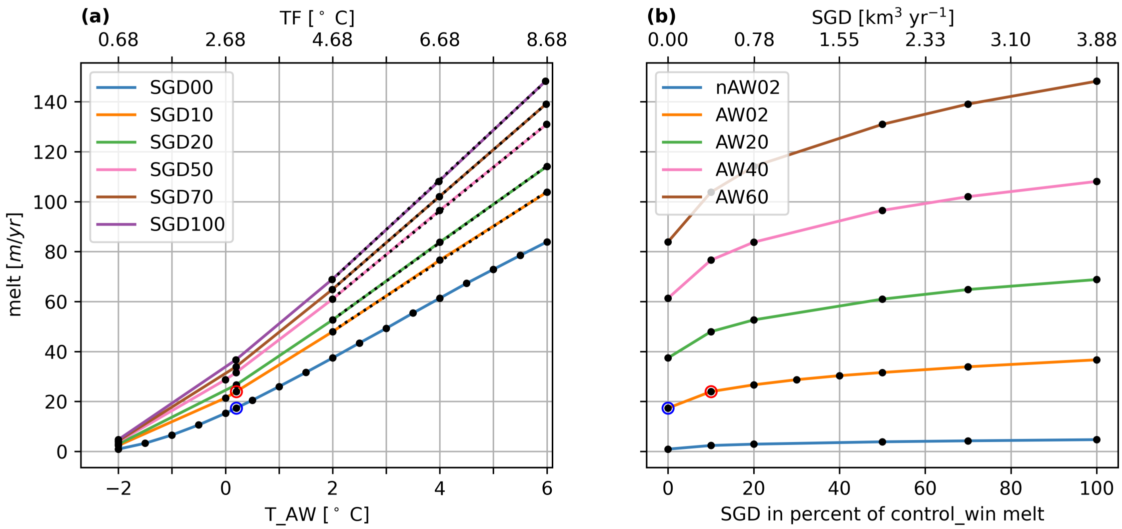

Figure 8. (a) The average melt (left ordinate axis) as a function of AW temperatures (T_{AW}; bottom abscissa) corresponding to ~~thermal~~ temperature forcing (TF; top abscissa) for ~~summer experiments~~ for summer model experiments with added ~~SDG~~ SGD (dots). The colored lines link model simulations with equal SGD. Dotted lines, superimposed on the colored lines show the linear regression models for the respective SGD experiments. (b) The average melt as a function of SGD (dots). The colored lines indicate sets of experiments with equal ~~thermal forcing~~AW temperature. The blue and red circles indicate winter and summer control simulations, respectively.

to an increase of 11.71m yr^{-1} K^{-1} for no SGD. Beware, that for SGD experiments the fit is only calculated for the three available data points with TF≥3.18°C.

3. For experiments with constant TF, the melt rates ~~increases~~ increase less than linear (in a fractional manner) with ~~the~~ SGD (Figure ~~8b).~~ 7b). The exponents c in the relationship between melt rate M and SGD volume V_{SGD}, M=a+bV^c_{sgd}, are 0.41 for SGD experiments with TF≈0.68°C (*_*nAW20*, 5 experiments), 0.46 for SGD experiments with TF≈2.87°C (*_*AW02*, 5 experiments) and TF≈4.67°C (*_*AW20*, 5 experiments) and 0.47 for SGD experiments with TF≈6.65°C (*_*AW40*, 5 experiments) and TF=8.67°C (*_*AW60*, 5 experiments). Using the additional experiments available for *_*AW02* experiments the exponent is 0.45 (7 experiments), showing some sensitivity of the fit to the number of data pairs used within a fixed range.

3.4 Comparison with 1-D plume model

A comparison between ocean circulation model results and those from the 1-D idealized plume model (Jenkins, 1991, 2011) is not straightforward. An ocean circulation model, like MITgcm, includes for example non-linear and viscous terms and resolves the plume with several grid points in the vertical, whereas the 1-D model simulates a uniform (in the normal direction to the ice) plume. Nevertheless, we compare the resulting melt rates of both models here, as the plume model is a well known and

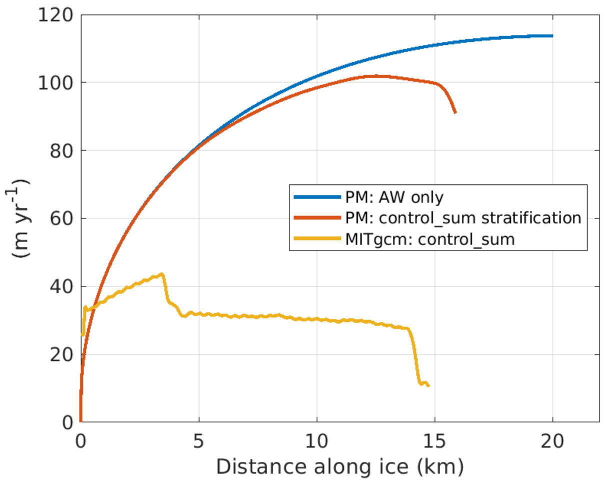

Figure 9. Melt rates from the plume model ("PM") using a uniform profile with AW temperature and salinity (blue, "AW only") and the simulated steady state ambient temperature and salinity profiles from the MITgcm control_sum simulation outside the ice shelf cavity (red, "*control_sum* stratification") as ambient water properties. In yellow, the melt rate from MITgcm *control_sum* simulation.

established tool to estimate melt rates. In Figure 9 we compare melt rates from our *control_sum* simulation with those from the 1-D Jenkins plume model. The plume model is set up with the same ice geometry and the steady state temperature and salinity profile outside the ice shelf cavity at x=21 km from the MITgcm simulation (*control_sum*) as the ambient water properties. To investigate the sensitivity to ambient stratification we also run the plume model with uniform ambient properties of AW only. We apply the same SGD flux and channel height (20 m, see section 2) as in *control_sum*. Entrainment and drag coefficients are taken directly from Jenkins (2011). For a detailed description of the plume model see Jenkins (1991) and Jenkins (2011) and for a detailed description of the setup, please refer to the supplementary material of Jakobsson et al. (2020).

The MITgcm simulation shows around three times lower melt rates than the plume model. This can be explained by higher velocities in the plume model (not shown) and could be tuned by changing for example the drag coefficient or the entrainment coefficient (see e.g. Dansereau et al. (2013); Cai et al. (2017); Slater et al. (2022)). Since the area averaged melt rates in our simulations are comparable to those from satellite observations (Wilson et al. (2017), see Section 4) we do not attempt any tuning of the MITgcm simulations to the plume model. Importantly, both models show the sensitivity to the stratification (compare "uniform stratification" and "simulated stratification" in figure 9), namely a shift in melt rates, that is described in Section 3.1 and discussed below (Section 4).

4 Discussion and conclusions

We used a high resolution, ~~non-hydrostatic~~ nonhydrostatic configuration of the MITgcm to investigate basal melt rates and melt driven circulation in a fjord with an ice tongue. The fjord–ice-tongue geometry is highly idealized, but the grounding-line depth and ice-tongue length are selected to represent ~~Ryder Glacier in Sherard Osborn Fjord~~RG in SOF, northwestern Greenland. The basal geometry of Ryder's ice tongue varies across the fjord, a feature that cannot be represented in the present two-dimensional model. For simplicity, we have chosen an ice-tongue with a linear basal slope, which roughly corresponds to the area-averaged basal slope of Ryder. The control model configuration is based on the observational survey of the *Ryder 2019 Expedition* and, to our knowledge, our study is the first to investigate aspects of this glacier–fjord system using high-resolution ocean modelling. A protocol of model sensitivity experiments quantified the response to oceanic thermal forcing due to warming Atlantic Water (AW), and to the buoyancy input from the ~~subglacial discharge (SGD)~~ SGD of surface fresh water. We applied broad ranges of varying AW temperatures and ~~SDG~~ SGD fluxes to better resolve the basal melt response to forcing and to make our model experiment more universal and relevant to future development of basal melt parameterizations in climate ice sheet models.

Model representation of the glacier-fjord system

Our control simulations represent salient features of estuarine circulation typical of Greenlandic glacier–fjord systems subject to oceanic thermal forcing due to the AW inflow (Straneo and Cenedese, 2015): the warm AW inflow in the deeper layer supplies heat to the ice base forcing basal melting. The melt water is fresher than ambient and drives a buoyant plume underneath the ice tongue. The plume rises into the base of the pycnocline where it reaches its level of neutral buoyancy, detaches from the glacier front, and intrudes horizontally into the ambient water forming an outflow jet back towards the open boundary. The entrainment of ambient water in the rising buoyant plume drives a slow flow of ambient waters toward the glacier.

The simulated melt rates for our idealized Ryder ~~Ice Tongue~~ice tongue, which has a linear basal slope, are broadly comparable to the satellite-derived ~~estimate~~ estimates from the real Ryder ice tongue for 2011–2015 by Wilson et al. (2017): our maximum melt rates in the summer control simulation near the grounding line are 40–50 m yr^{-1}, as in the observations while they are ~~slightly higher (around 20~~ around 20–30 m yr^{-1} ~~)~~ away from the grounding line compared to the observed ~~(~~10–20 m yr^{-1}~~)~~. The area-integrated basal melt for the control winter experiment (taking the ice tongue width of 8.5 km) is about 3 km^3 yr^{-1} as compared to the observed 1.8±0.21 km^3 yr^{-1} (Wilson et al., 2017), ~~while it is higher,~~ and about 4 km^3 yr^{-1}, for the summer control experiment (Table **??**). The simulated steady state fjord stratification recovers the observed signature of an outflow of glacially-modified water, which was smoothed out in the profiles used for initialization, providing additional qualitative support for the ~~feasability~~ feasibility of our model approach (Figure 1d and 3b).

Spatial structure of basal melt rates and melt driven circulation

Our high resolution model simulation allowed to resolve a spatial pattern of the basal melt and the melt driven circulation under the ice tongue. In the winter control simulation, the basal melt rates and the plume exhibit a two-regime structure along the ice base (high melt rates in the accelerating plume regime up to 7 km and the lower melt rates in thickening plume regime thereafter up to 14 km). This two regime structure is insensitive to the way of defining the plume (by buoyancy or velocity). We have diagnosed various plume diagnostics using a velocity criterion, which led to e.g. average plume thicknesses of around 40 m, comparable with what was found in Holland et al. (2008b). Care has to be taken, when comparing these diagnostics to the one dimensional plume model (Jenkins, 2011), where uniform plume properties are assumed. This is not necessarily true in the plume defined using the horizontal velocity. Adding a buoyancy criterion yields a narrower and faster plume (see Section 3.1), with almost uniform distribution of buoyancy. The uneven vertical spreading of momentum and tracers (i.e. temperature and salinity) can be attributed to a vertical Prandtl number larger than unity, which leads to a stronger downward diffusion of momentum away from the ice, increasing the region of positive horizontal velocities beyond the region of uniform buoyancy. The increased viscosity is needed in order to obtain stable simulations; increased tracer diffusivity would lead to a smearing out of the thermocline. To our knowledge, small-scale variations in the melt rate have been barely captured by observations (Wilson et al., 2017).

The two-regime structure persists in the sensitivity model runs with varying ocean thermal forcing. Applying an additional buoyancy source in simulations with SGD shifts the transition between the two regimes closer to the grounding line. Our results suggest that this spatial structure of the basal melt rates and the melt driven circulation is determined by the ambient density stratification as shifts of the transition zone in various sensitivity experiments ~~relates~~ relate to the downward ~~shift~~ shifts of the pycnocline and ~~shift~~ shifts in buoyancy forcing. Notably, in the first regime close to the grounding line, our simulated melt rates in the winter runs (without SGD) show a monotonic increase rather than a broader maximum found in Petermann Glacier simulations of Cai et al. (2017) (their Figure 2). This monotonic increase is less pronounced in our simulations with SGD (SGD was applied in ~~their study~~Cai et al. (2017)) but it could also be attributed to different ice geometry (a steep ice base close to the grounding line in their study, which would lead to increased melt rates there). Other factors that could affect the structure of the melt rates, but are unresolved by either modelling study, are the variability of the SGD in the transverse direction as it enters the fjord waters through channels discharging at the base of the glacier's front whose number, sizes, and geometries and time variability are mostly unknown and possibly influenced by the complex networks of drainage channels and crevasses in the glaciers (Chen, 2014) and the presence of basal channels and terraces (Millgate et al., 2013; Dutrieux et al., 2014).

Response to oceanic thermal forcing

In this study, we investigated the response of the melt rates and melt driven circulation to the oceanic thermal forcing ~~, TF~~ (varying AW temperatures). The form of the applied basal melt parametrization (Eqs. 2-3) suggests a non-linear dependence of the basal melt on TF, since the melt rate depends on both ~~,~~ the ocean temperature and the plume velocity through the transfer coefficient (Eq. 5). The plume velocity is in turn dependent on TF through the buoyancy input from the melt (Holland et al., 2008a; Jenkins, 2011; Lazeroms et al., 2018). A nonlinear relation was found in former studies of Antarctic ice shelves subject to ocean water temperatures around zero degrees (Holland et al., 2008b). Jenkins (2011) found a transition into a linear response of melt rate on TF for sufficiently high buoyancy input through strong SGD. On the other hand, several modelling studies of vertical tidewater glaciers around Greenland, where ocean temperatures are higher due to the AW inflow, have reported on a linear dependency of melt rates on TF (Xu et al., 2012; Sciascia et al., 2013, 2014). A modelling study of Petermann Glacier, a neighbour of ~~Ryder Glacier~~RG, by Cai et al. (2017) found a slightly non-linear dependency of melt on TF using a similar set of sensitivity experiments as presented here and assuming the same relationship for the whole TF range.

Here, we applied a wide range of oceanic thermal forcing (with T_{AW} up to 6° C, i.e., higher than typically observed at the Greenland's marine terminating glaciers, see e.g. Straneo and Cenedese (2015)) and a resampling technique to quantify the response of the melt rate and the resulting circulation to varying TF ~~in more detail~~with a higher statistical confidence. We found that a non-linear relationship holds for the simulations with low TF (TF$\leq$ 2.88° C, Figure 5a), while it becomes linear for higher TF, thus ~~unifying~~ linking up and contextualizing results from the previous studies. Note that using a fully nonlinear EOS instead of the linear approximation (Equation 1) is unlikely to change our results about the dependency of melt on TF. At the lower ocean temperature range, the difference between a linear and nonlinear EOS is insignificant. At the AW temperatures > 0° C, the effect of ambient ocean temperature on the plume buoyancy described above is expected to be further enhanced with a nonlinear EOS. A previous study of Sciascia et al. (2013) for example, did use a nonlinear EOS and found a linear dependence of melt on TF for the AW temperatures they considered (0 - 8° C), consistent with our result for this range.

We went further in trying to elucidate ~~this~~ the aforementioned regime shift in the melt rate response to oceanic thermal forcing by examining the buoyancy forcing of the melt driven plume. For cold ambient temperatures the plume buoyancy is dominated by the salinity difference between the plume and the ambient water~~, and this salinity difference increases slowly with TFdue to the increased melt water flux to the fjord.The increasing ambient water temperaturehowever, leads to increasing temperature difference between the plume and the ambient water~~. For increasing TF, i.e. increasing ambient temperature, ~~leading to a negative effect on the plumes buoyancy. For sufficiently warm ambient temperatures (i.e., high TF) , the negative effect due to increasing ambient water temperature difference on the buoyancy overrides the positive effect of freshening from increased input of melt water (Figure b)~~the following mechanisms are in place. First, the melt rate increases leading to higher input of fresh and cold melt water. Second, the cooling due to mixing of the ambient AW becomes more efficient because of the larger temperature gradient between the (warmer) ambient water and melt water. Hence the cooling close to the ice boundary increases stronger than the freshening with increasing TF. In figure 4b this manifests in the slopes of "Buo-S" and "Buo-T" becoming approximately the same for higher TF. Since salinity and temperature effect are of opposite sign, the net change in buoyancy in the plume with increasing TF diminishes, leading to a flattening of the slope of "Buo". As a consequence, the plume velocities do not increase further with TF (Figure 5b), resulting in effectively constant exchange coefficient in (Eq. 3) and a linear dependence of melt rates for higher TF. An additional factor could be the dependence of T_b (Eqn. 2) and therefore the heat balance (Eqn. 3) on S_b. An increased melt rate due to higher TF will decrease salinity at the interface, thereby increasing T_b and decreasing the local temperature difference ($T_w - T_b$) along the ice. This could potentially be a negative feedback on the melt rate contributing to the observed change in dependency of the melt rate on TF from non-linear to linear at higher TF. These results are generic and relevant for future development of the basal melt parameterizations for marine terminating glaciers in the climate ice sheet models.

Response to subglacial discharge

SGD, the buoyant freshwater released at depth from under Greenland's marine-terminating glaciers, is sourced largely from atmospheric-driven melting of the ice sheet surface during the summer (Chen, 2014). SGD provides an additional buoyancy source for the plume underneath the ice tongue, leading to higher basal melt rates due to higher plume velocities and entrainment of the ambient warm water (Straneo and Cenedese, 2015). Thus, submarine melting integrates both oceanic and atmospheric influences. A recent study of the relative importance of oceanic and atmospheric drivers of submarine melting at Greenland's marine-terminating glaciers from 1979 to 2018 concluded that in the north, the ~~subglacial discharge~~ SGD is at least as important as variability in the oceanic thermal forcing to submarine melt rates, while it exhibits an order of magnitude larger variability on decadal time scales (Slater and Straneo, 2022). Here, we considered the response of the basal melt and melt driven circulation to varying SGD rates. In lieu of missing accurate observational estimates of ~~SDG~~SGD, we set it to be a fraction of the total basal melt for the winter control simulation.

We found that the ~~subglacial discharge (SGD)~~ SGD has a pronounced effect on the basal melt rates. The average melt rate for the summer control simulations (where SGD is set to $\approx$10% of the average basal melt flux for the control winter), is increased by 38%, and for the experiment with the the SGD input set to 100% of the average winter melt rate the increase in melt is 111%, consistent with the conclusions of Slater and Straneo (2022) for ~~the northern Greenland.~~ northern Greenland, that there is large seasonal variability in melt rate due to atmospheric forcing through SGD. Given that the SGD values presented here are still lower than the average SGD reported by Slater et al. (2022) for June, July and August, we would expect very high seasonal variability in melt rate at north Greenland's ice shelves. The additional buoyancy input affects the distribution of the melt rates and plume properties along the ice base, enhancing the melt rate and shifting the transition zone between the plume accelerating and thickening regimes closer to the grounding line. This shift of transition zone collocates with a downward thickening of the pycnocline. The functional response of the melt rate to TF found in the winter simulations (without SGD, see above) holds for the simulations with SGD, but there is stronger linear increase in the melt rate with TF for experiments with SGD as compared to the experiments without SGD. For experiments with constant TF, the melt rates increase less than linear (in a fractional manner) with the SGD, consistent with the modelling experiments of (Cai et al., 2017) for Petermann Glacier and the theoretical scaling of ~~Slater et al. (2016).~~ Jenkins (2011) and Slater et al. (2016). Our values for the exponent vary between 0.4 and 0.5 for the different experiments; they are slightly higher than what is estimated from theory (1/3) and close to those found by Sciascia et al. (2013) (0.33-0.5) and Cai et al. (2017) (0.56).

Future outlook

In this work, we have focused on basal melt rates and melt driven circulation in the ice cavity under the floating tongue of ~~Ryder Glacier~~RG, with restoring to a prescribed ocean stratification at the open boundary 30 km upstream. There are several important aspects considering the model representation of these processes. One is the sensitivity to the model resolution and viscosity/diffusivity. In previous studies using MITgcm in similar applications and resolutions Sciascia et al. (2013) and in particular Xu et al. (2012) found that while the plume got better resolved and the average melt rates increased for higher resolution, the general circulation pattern and results about the dependency on oceanic forcing and SGD were consistent between the different simulations. Similar sensitivities to the vertical resolution and the parametrization of melt processes in different vertical coordinate models are found in other models as well, as shown recently by Gwyther et al. (2020). They conclude that the most realistic representation remains unknown and results always have to be considered with respect to the implementation used.

On the other hand, the melt rate magnitude depends also on other factors e.g., the friction coefficient (Dansereau et al., 2013), which was used by Cai et al. (2017) to tune the model to the observed melt rates, rather than the model resolution. In our simulation with sloping ice shelf, both vertical and horizontal resolution (and viscosity/diffusivity) need to be taken into consideration in a dedicated sensitivity study, and not only the effects on basal melt but also on the representation of the stratification and the mixing between the two water masses, AW and PSW in the domain will influence the ocean heat transport to the ice-ocean interface.

Future work will include the influence of sill bathymetry in the 100 km long ~~Sherard Osborn Fjord~~ SOF on the oceanic heat transport to the ice cavity. Other important factors to be considered are the spatial and temporal variability of the SGD (Chen, 2014) and the three-dimensional geometry of the ice base featuring a presence of basal channels and terraces (Millgate et al., 2013; Dutrieux et al., 2014). Including these factors in modelling studies is however contingent upon collecting accurate observational estimates necessary to initialize and evaluate the models.

Code and data availability. Setup files necessary to reproduce the simulations using the MITgcm, (https://github.com/MITgcm/MITgcm/releases/tag/checkpoint67s) are uploaded to the Bolin Research Centre Data Centre under https://git.bolin.su.se/bolin/wiskandt-2023-ryder-melt.

Appendix A: Overview Experiments

Table A1. Setup parameters and characteristic diagnostics for temperature sensitivity experiments. From left to right: Atlantic Water Temperature, subglacial discharge volume in percent of *control_win* integrated melt volume, model time step, ~~temperature forcing~~TF, overturning time scale, averaged melt rate~~/ ice retreat~~, integrated melt ~~(calculated~~ for ~~two dimensional melt)~~a 10km wide fjord.

ExpName	T_{AW} [°C]	SGD Vol. [km^3 yr^{-1}]	dt [s]	TF [°C]	τ_o [days]	Ave. Melt [m yr^{-1}]	Melt Flux [km^3 yr^{-1}]
nAW20	-2.0	0.00	10	0.68	78	0.92	0.18
nAW15	-1.5	0.00	10	1.18	44	3.26	0.65
nAW10	-1.0	0.00	10	1.68	34	6.56	1.31
nAW05	-0.5	0.00	10	2.18	30	10.62	2.12
AW00	-0.0	0.00	10	2.68	27	15.28	3.06
control_win	0.2	0.00	10	2.87	27	17.36	3.47
AW05	0.5	0.00	10	3.17	25	20.48	4.10
AW10	1.0	0.00	10	3.67	24	25.97	5.19
AW15	1.5	0.00	10	4.17	24	31.62	6.32
AW20	2.0	0.00	10	4.67	23	37.43	7.49
AW25	2.5	0.00	10	5.17	23	43.40	8.68
AW30	3.0	0.00	10	5.66	22	49.28	9.86
AW35	3.5	0.00	5	6.16	22	55.40	11.08
AW40	4.0	0.00	5	6.66	22	61.34	12.27
AW45	4.5	0.00	5	7.16	22	67.31	13.46
AW50	5.0	0.00	5	7.66	22	72.90	14.58
AW55	5.5	0.00	5	8.15	22	78.47	15.69
AW60	6.0	0.00	5	8.65	22	83.91	16.78

Table A2. Setup parameters and characteristic diagnostics for subglacial discharge sensitivity experiments. From left to right: Atlantic Water Temperature, subglacial discharge volume in percent of *control_win* integrated melt volume, model time step, ~~temperature forcing~~TF, overturning time scale, averaged melt rate~~/ ice retreat~~, integrated melt ~~(calculated~~ for ~~two dimensional melt)~~a 10km wide fjord.

ExpName	T_{AW} [°C]	SGD Vol. [km^3 yr^{-1}]	dt [s]	TF [°C]	τ_o [days]	Ave. Melt [m yr^{-1}]	Melt Flux [km^3 yr^{-1}]
sgd010_nAW20	-2.0	0.39	5	0.68	23	2.37	0.47
sgd020_nAW20	-2.0	0.78	5	0.68	18	2.90	0.58
sgd050_nAW20	-2.0	1.94	5	0.69	14	3.85	0.77
sgd070_nAW20	-2.0	2.72	3	0.69	12	4.24	0.85
sgd100_nAW20	-2.0	3.88	3	0.69	11	4.71	0.94
sgd010_AW00	-0.0	0.39	5	2.67	18	21.41	4.28
sgd050_AW00	-0.0	1.94	5	2.67	12	28.69	5.74
control_sum	0.2	0.39	5	2.87	18	23.96	4.79
sgd020_AW02	0.2	0.78	5	2.87	15	26.67	5.34
sgd030_AW02	0.2	1.16	5	2.87	14	28.73	5.75
sgd040_AW02	0.2	1.55	5	2.87	13	30.33	6.07
sgd050_AW02	0.2	1.94	5	2.87	12	31.60	6.32
sgd070_AW02	0.2	2.72	3	2.86	11	33.89	6.78
sgd100_AW02	0.2	3.88	3	2.86	10	36.67	7.34
sgd010_AW20	2.0	0.39	5	4.67	17	47.96	9.60
sgd020_AW20	2.0	0.78	5	4.66	15	52.67	10.54
sgd050_AW20	2.0	1.94	4	4.65	12	60.98	12.20
sgd070_AW20	2.0	2.72	3	4.64	11	64.82	12.97
sgd100_AW20	2.0	3.88	3	4.63	10	68.82	13.77
sgd010_AW40	4.0	0.39	5	6.65	16	76.59	15.33
sgd020_AW40	4.0	0.78	5	6.65	15	83.78	16.77
sgd050_AW40	4.0	1.94	5	6.63	12	96.52	19.31
sgd070_AW40	4.0	2.72	3	6.62	11	102.01	20.41
sgd100_AW40	4.0	3.88	3	6.60	10	108.11	21.63
sgd010_AW60	6.0	0.39	5	8.65	16	103.81	20.77
sgd020_AW60	6.0	0.78	5	8.63	15	114.13	22.84
sgd050_AW60	6.0	1.94	5	8.61	12	130.97	26.21
sgd070_AW60	6.0	2.72	2	8.59	11	139.10	27.83
sgd100_AW60	6.0	3.88	2	8.57	10	148.24	29.66

Appendix B: ~~Time series~~Supplementary Figures

Time series show that for all experiments key diagnostics stabilize after 20-40 days (Figure B1 and B2). Only the integrated temperature change is increasing with time for high AW temperature experiments after an initial strong decrease (Figure B1). This increase can be attributed to a heating up of the upper layer of polar water from below. Because all other diagnostics show a statistical steady state, we can assume that the increase in heat does not influence the circulation we are investigating.

Figure B3 shows in colors the buoyancy (a) and velocity (b) in the plume of the *control_win* simulation. The white line indicates the isoline of the 75th precentile of buoyancy. Compare to section 3.1

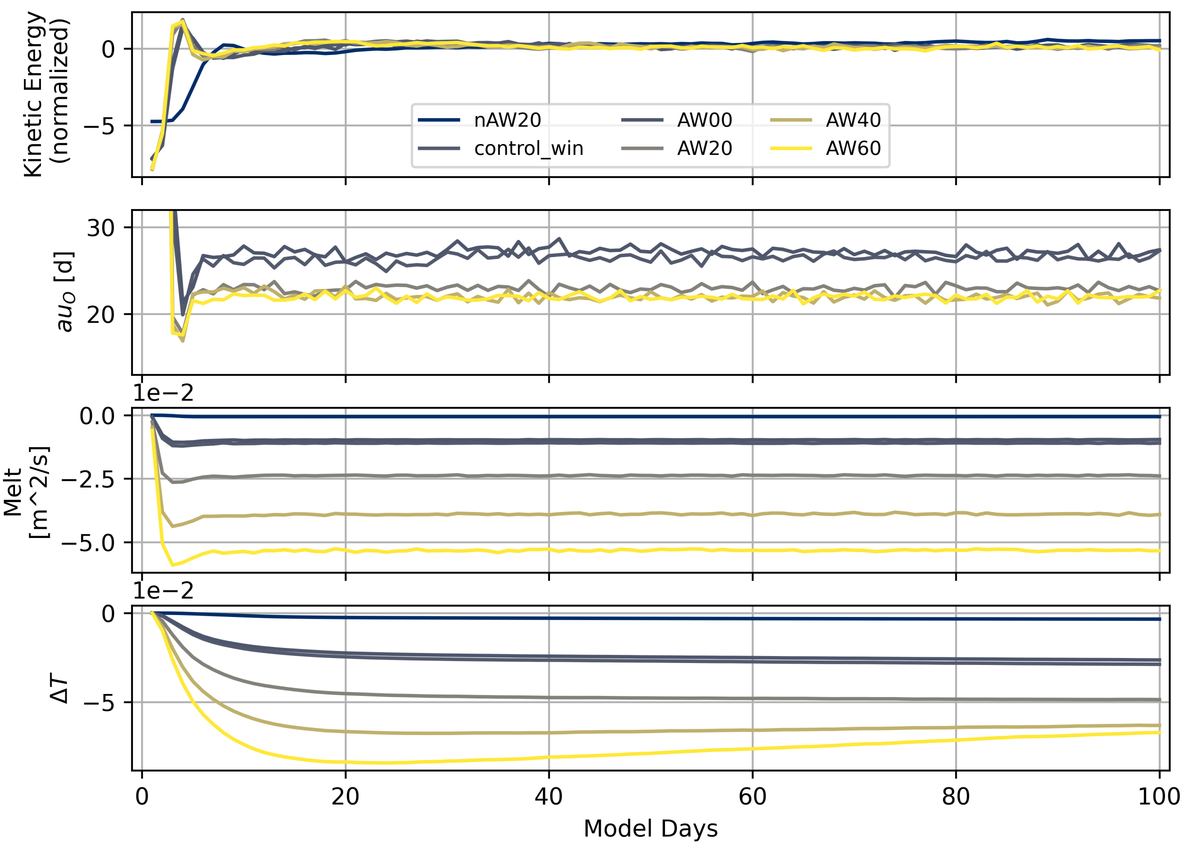

Figure B1. From top to bottom: Kinetic Energy, overturning timescale, melt flux (solid) and integrated temperature change (compared to initial state) as functions of model Days; shown for a representative subset of temperature sensitivity experiments.

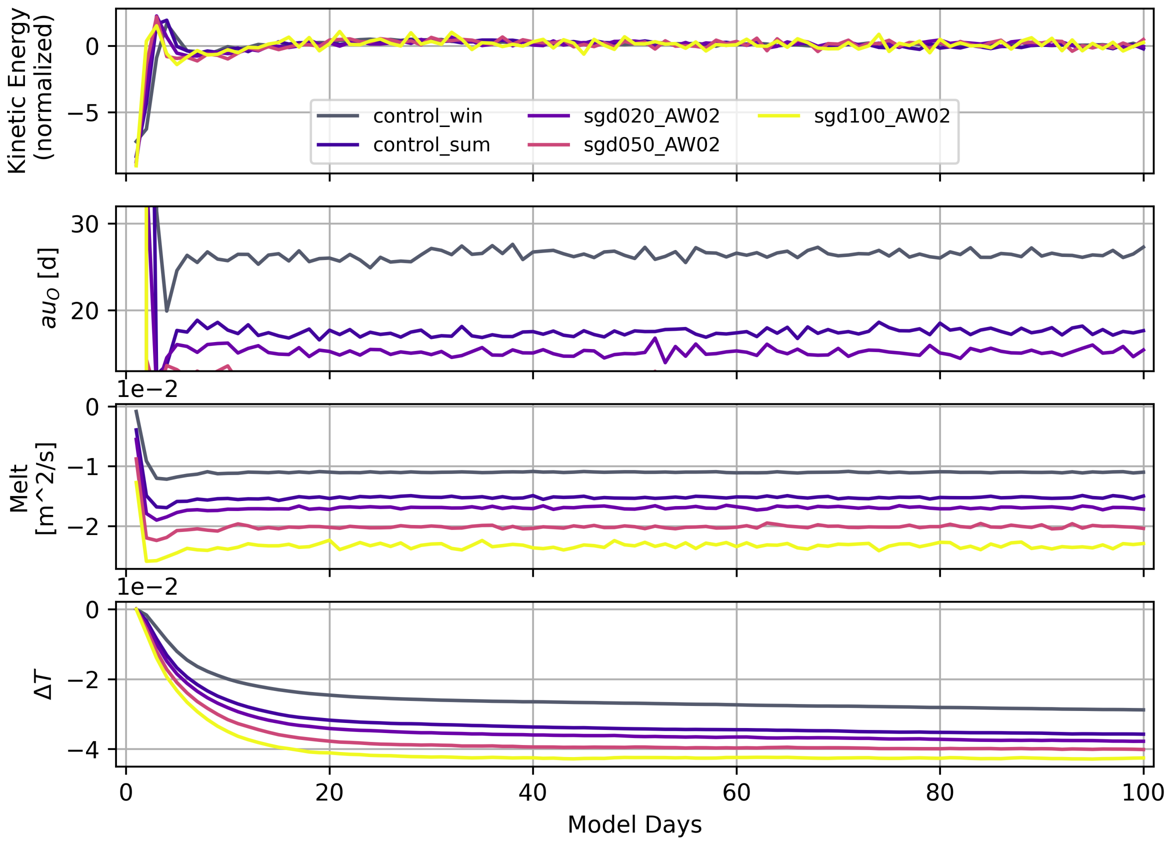

Figure B2. From top to bottom: Kinetic Energy, overturning timescale, melt flux (solid) and integrated temperature change (compared to initial state) as functions of model Days; shown for a representative subset of subglacial discharge sensitivity experiments.

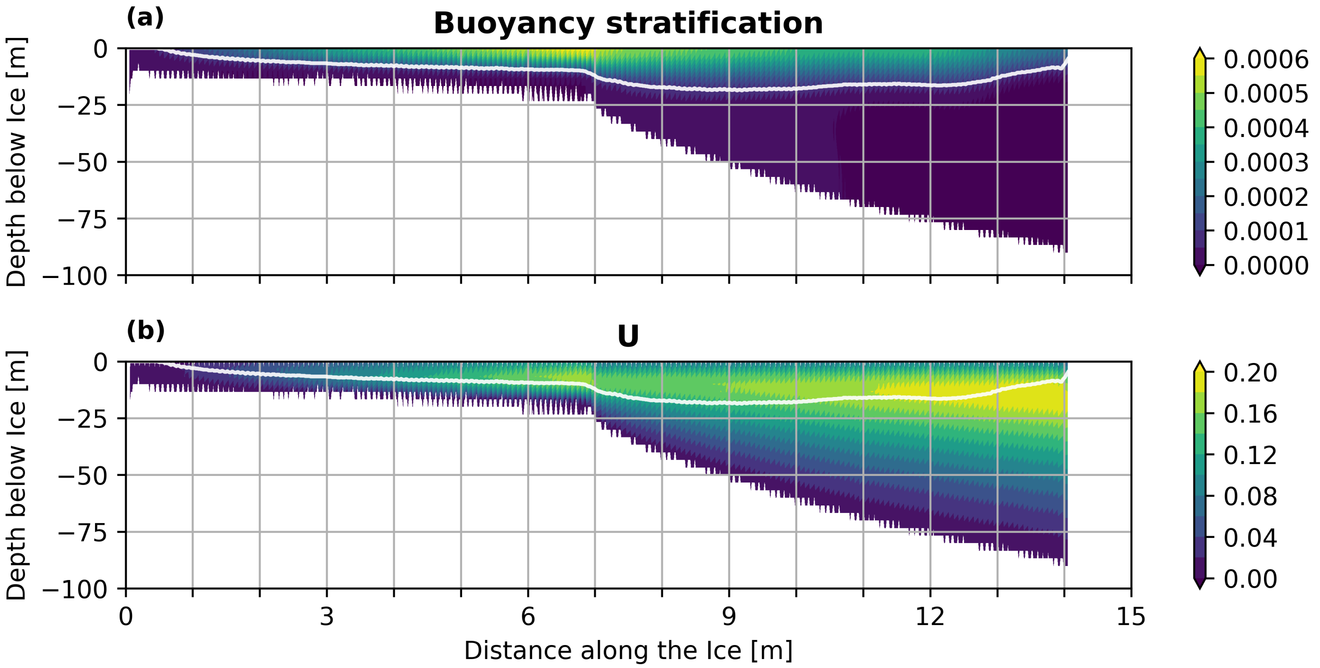

Figure B3. Section of buoyancy (a) and along ice velocity (b) within the plume region, as defined by the horizontal velocity criterion (u>0). The white lines indicate the 75th percentile buoyancy isoline.

Author contributions. JW conducted the model simulations and data analysis with support of IMK and JN. IMK and JN contributed to experiment setup and the interpretation of the results. JW wrote the manuscript and all authors contributed to correcting and editing the final version.

Competing interests. The authors declare that they have no conflict of interest.

Acknowledgements. This work was performed within a pair PhD project funded by the Faculty of Science, Stockholm University, and granted to the Department of Mathematics, division of Computational Mathematics, and the Department of Meteorology (SUFV-1.2.1-0124-17). The computations and data analysis were enabled by resources provided by the Swedish National Infrastructure for Computing (SNIC) at the National Supercomputer Centre (NSC), partially funded by the Swedish Research Council through grant agreement no. 2018-05973. The Authors would like to thank Roberta Sciascia for fruitfull discussions.

References

Adcroft, A. J., Hill, C., Campin, J. M., Marshall, J., and Heimbach, P.: Overview of the formulation and numerics of the MIT GCM, in: Proceedings of the ECMWF seminar series on Numerical Methods, Recent developments in numerical methods for atmosphere and ocean modelling, pp. 139–149, ECMWF, URL: https://www.ecmwf.int/en/elibrary/7642-overview-formulation-and-numerics-mit-gcm, 2004.

Asay-Davis, X., Jourdain, N., and Nakayama, Y.: Developments in Simulating and Parameterizing Interactions Between the Southern Ocean and the Antarctic Ice Sheet, Curr. Clim. Change Rep., 3, 316–329, https://doi.org/https://doi.org/10.1007/s40641-017-0071-0, 2017.

Asay-Davis, X. S., Cornford, S. L., Durand, G., Galton-Fenzi, B. K., Gladstone, R. M., Hilmar Gudmundsson, G., Hattermann, T., Holland, D. M., Holland, D., Holland, P. R., Martin, D. F., Mathiot, P., Pattyn, F., and Seroussi, H.: Experimental design for three interrelated marine ice sheet and ocean model intercomparison projects: MISMIP v. 3 (MISMIP +), ISOMIP v. 2 (ISOMIP +) and MISOMIP v. 1 (MISOMIP1), Geoscientific Model Development, 9, 2471–2497, https://doi.org/10.5194/gmd-9-2471-2016, 2016.

Boning, C. W., Behrens, E., Biastoch, A., Getzlaff, K., and Bamber, J. L.: Emerging impact of Greenland meltwater on deepwater formation in the North Atlantic Ocean, Nature Geoscience, 9, 523–527, https://doi.org/10.1038/ngeo2740, 2016.

Bradley, A. T., Williams, C. R., Jenkins, A., and Arthern, R.: Asymptotic Analysis of Subglacial Plumes in Stratified Environments, http://arxiv.org/abs/2103.09003, 2021.

Burchard, H., Bolding, K., Jenkins, A., Losch, M., Reinert, M., and Umlauf, L.: The Vertical Structure and Entrainment of Subglacial Melt Water Plumes, Journal of Advances in Modeling Earth Systems, 14, 1–34, https://doi.org/10.1029/2021MS002925, 2022.

Cai, C., Rignot, E., Menemenlis, D., and Nakayama, Y.: Observations and modeling of ocean-induced melt beneath Petermann Glacier Ice Shelf in northwestern Greenland, Geophysical Research Letters, 44, 8396–8403, https://doi.org/10.1002/2017GL073711, 2017.

Carroll, D., Sutherland, D. A., Shroyer, E. L., Nash, J. D., Catania, G. A., and Stearns, L. A.: Modeling turbulent subglacial meltwater plumes: Implications for fjord-scale buoyancy-driven circulation, Journal of Physical Oceanography, 45, 2169–2185, https://doi.org/10.1175/JPO-D-15-0033.1, 2015.

Chen, V.: Greenland ice sheet hydrology: a review, Prog. Phys. Geogr. Earth Environ., 38, 19–54, 2014.

Choi, Y., Morlighem, M., Rignot, E., Mouginot, J., and Wood, M.: Modeling the Response of Nioghalvfjerdsfjorden and Zachariae Isstrøm Glaciers, Greenland,to Ocean Forcing Over the Next Century, Geophys. Res. Lett, 44, 11,071–11,079, 2017.

Cowton, T., Slater, D., Sole, A., Goldberg, D., and Nienow, P.: Modeling the impact of glacial runoff on fjord circulation and submarine melt rate using a new subgrid-scale parameterization for glacial plumes, Journal of Geophysical Research: Oceans, 120, 796–812, https://doi.org/10.1002/2014JC010324, 2015.

Dansereau, V., Heimbach, P., and Losch, M.: Journal of Geophysical Research : Oceans, Journal of Geophysical Research: Oceans, 2001, 1–26, https://doi.org/10.1002/2013JC008846.Received, 2013.

Dutrieux, P., Stewart, C., Jenkins, A., Nicholls, K. W., Corr, H. F. J., Rignot, E., and Steffen, K.: Basal terraces on melting ice shelves, Geophys. Res. Lett., 41, 5506–5513, 2014.

Edwards, T. L., Fettweis, X., Gagliardini, O., Gillet-Chaulet, F., Goelzer, H., Gregory, J. M., Hoffman, M., Huybrechts, P., Payne, A. J., Perego, M., Price, S., Quiquet, A., and Ritz, C.: Probabilistic parameterisation of the surface mass balance–elevation feedback in regional climate model simulations of the Greenland ice sheet, The Cryosphere, 8, 181–194, https://doi.org/10.5194/tc-8-181-2014, 2014.

Enderlin, E. M. and Howat, I. M.: Submarine melt rate estimates for floating termini of Greenland outlet glaciers (2000–2010), Journal of Glaciology, 59, 67–75, https://doi.org/10.3189/2013JoG12J049, 2013.

Enderlin, E. M., Howat, I. M., Jeong, S., Noh, M., van Angelen, J. H., and van den Broeke, M. R.: An improved mass budget for the Greenland ice sheet, Geophysical Research Letters, 41, 866–872, https://doi.org/10.1002/2013GL059010, 2014.

Fox-Kemper, B., Hewitt, H. T., Xiao, C., Aðalgeirsdóttir, G., Drijfhout, S. S., Edwards, T. L., Golledge, N. R., Hemer, M., Kopp, R. E., Krinner, G., Mix, A., Notz, D., Nowicki, S., Nurhati, I. S., Ruiz, L., Sallée, J.-B., Slangen, A. B. A., and Yu, Y.: Ocean, Cryosphere and Sea Level Change, in: Climate Change 2021: The Physical Science Basis. Contribution of Working Group I to the Sixth Assessment Report of the Intergovernmental Panel on Climate Change, edited by Masson-Delmotte, V., Zhai, P., Pirani, A., Connors, S. L., Péan, C., Berger, S., Caud, N., Chen, Y., Goldfarb, L., Gomis, M. I., Huang, M., Leitzell, K., Lonnoy, E., Matthews, J. B. R., Maycock, T. K., Waterfield, T., Yelekçi, O., Yu, R., and Zhou, B., p. 1211–1362, Cambridge University Press, Cambridge, United Kingdom and New York, NY, USA, https://doi.org/10.1017/9781009157896.011, 2021.

Gelderloos, R., Haine, T. W. N., Koszalka, I. M., and Magaldi, M. G.: Seasonal Variability in Warm-Water Inflow toward Kangerdlugssuaq Fjord, Journal of Physical Oceanography, 47, 1685 – 1699, https://doi.org/10.1175/JPO-D-16-0202.1, 2017.

Gudmundsson, G. H.: Ice-shelf buttressing and the stability of marine ice sheets, Cryosphere, 7, 647–655, https://doi.org/10.5194/tc-7-647-2013, 2013.

Gwyther, D. E., Kusahara, K., Asay-Davis, X. S., Dinniman, M. S., and Galton-Fenzi, B. K.: Vertical processes and resolution impact ice shelf basal melting: A multi-model study, Ocean Modelling, 147, 101 569, https://doi.org/10.1016/j.ocemod.2020.101569, 2020.

Hellmer, H. and Olbers, D.: A two-dimensional model for the thermohaline circulation under an ice shelf, Antarctic Science, 1, 325–336, https://doi.org/10.1017/S0954102089000490, 1989.

Hill, E. A., Rachel Carr, J., Stokes, C. R., and Hilmar Gudmundsson, G.: Dynamic changes in outlet glaciers in northern Greenland from 1948 to 2015, Cryosphere, 12, 3243–3263, https://doi.org/10.5194/tc-12-3243-2018, 2018.

Holland, D. M. and Jenkins, A.: Modeling thermodynamic ice-ocean interactions at the base of an ice shelf, Journal of Physical Oceanography, 29, 1787–1800, https://doi.org/10.1175/1520-0485(1999)029<1787:mtioia>2.0.co;2, 1999.

Holland, D. M., Thomas, R. H., de Young, B., Ribergaard, M. H., and Lyberth, B.: Acceleration of Jakobshavn Isbrae triggered by warm surbsurface ocean waters, Nature Geoscience, 1, 659–664, 2008a.

Holland, P. R., Jenkins, A., and Holland, D. M.: The response of Ice shelf basal melting to variations in ocean temperature, Journal of Climate, 21, 2558–2572, https://doi.org/10.1175/2007JCLI1909.1, 2008b.

Jakobsson, M., Mayer, L. A., Nilsson, J., Stranne, C., Calder, B., O'Regan, M., Farrell, J. W., Cronin, T. M., Brüchert, V., Chawarski, J., Eriksson, B., Fredriksson, J., Gemery, L., Glueder, A., Holmes, F. A., Jerram, K., Kirchner, N., Mix, A., Muchowski, J., Prakash, A., Reilly, B., Thornton, B., Ulfsbo, A., Weidner, E., Åkesson, H., Handl, T., Ståhl, E., Boze, L.-G., Reed, S., West, G., and Padman, J.: Ryder Glacier in northwest Greenland is shielded from warm Atlantic water by a bathymetric sill, Communications Earth & Environment, 1, 1–10, https://doi.org/10.1038/s43247-020-00043-0, 2020.

Jenkins, A.: A one-dimensional model of ice shelf-ocean interaction, Journal of Geophysical Research, 96, 20 671, https://doi.org/10.1029/91JC01842, 1991.

Jenkins, A.: Convection-driven melting near the grounding lines of ice shelves and tidewater glaciers, Journal of Physical Oceanography, 41, 2279–2294, https://doi.org/10.1175/JPO-D-11-03.1, 2011.

Jenkins, A., Nicholls, K. W., and Corr, H. F.: Observation and parameterization of ablation at the base of Ronne Ice Ahelf, Antarctica, Journal of Physical Oceanography, 40, 2298–2312, https://doi.org/10.1175/2010JPO4317.1, 2010.

Jordan, J. R., Holland, P. R., Goldberg, D., Snow, K., Arthern, R., Campin, J. M., Heimbach, P., and Jenkins, A.: Ocean-Forced Ice-Shelf Thinning in a Synchronously Coupled Ice-Ocean Model, Journal of Geophysical Research: Oceans, 123, 864–882, https://doi.org/10.1002/2017JC013251, 2018.

Koszalka, I. M., Haine, T. W. N., and Magaldi, M. G.: Fates and Travel Times of Denmark Strait Overflow Water in the Irminger Basin, Journal of Physical Oceanography, 43, 2611–2628, https://doi.org/https://doi.org/10.1175/JPO-D-13-023.1, 2013.

Lazeroms, W. M., Jenkins, A., Hilmar Gudmundsson, G., and Van De Wal, R. S.: Modelling present-day basal melt rates for Antarctic ice shelves using a parametrization of buoyant meltwater plumes, Cryosphere, 12, 49–70, https://doi.org/10.5194/tc-12-49-2018, 2018.

Lazeroms, W. M., Jenkins, A., Rienstra, S. W., and Van De Wal, R. S.: An analytical derivation of ice-shelf basal melt based on the dynamics of meltwater plumes, Journal of Physical Oceanography, 49, 917–939, https://doi.org/10.1175/JPO-D-18-0131.1, 2019.

Losch, M.: Modeling ice shelf cavities in a z coordinate ocean general circulation model, Journal of Geophysical Research: Oceans, 113, 1–15, https://doi.org/10.1029/2007JC004368, 2008.

Luo, H., Castelao, R. M., Rennermalm, A. K., Tedesco, M., Bracco, A., Yager, P. L., and Mote, T. L.: Oceanic transport of surface meltwater from the southern Greenland ice sheet, Nature Geoscience, 9, 528–532, https://doi.org/https://doi.org/10.1038/ngeo2708, 2016.

Mankoff, K. D., Noël, B., Fettweis, X., Ahlstrøm, A. P., Colgan, W., Kondo, K., Langley, K., Sugiyama, S., van As, D., and Fausto, R. S.: Greenland liquid water discharge from 1958 through 2019, Earth System Science Data, 12, 2811–2841, https://doi.org/10.5194/essd-12-2811-2020, 2020.

Marshall, J., Hill, C., Perelman, L., and Adcroft, A.: Hydrostatic, quasi-hydrostatic, and nonhydrostatic ocean modeling, Journal of Geophysical Research C: Oceans, 102, 5733–5752, https://doi.org/10.1029/96JC02776, 1997.

Mauritzen, C., Hansen, E., Andersson, M., Berx, B., Beszczynska-Möller, A., Burud, I., Christensen, K., Debernard, J., de Steur, L., Dodd, P., Gerland, S., Godøy, , Hansen, B., Hudson, S., Høydalsvik, F., Ingvaldsen, R., Isachsen, P., Kasajima, Y., Koszalka, I., Kovacs, K., Køltzow, M., LaCasce, J., Lee, C., Lavergne, T., Lydersen, C., Nicolaus, M., Nilsen, F., Nøst, O., Orvik, K., Reigstad, M., Schyberg, H., Seuthe, L., Skagseth, , Skarðhamar, J., Skogseth, R., Sperrevik, A., Svensen, C., Søiland, H., Teigen, S., Tverberg, V., and Wexels Riser, C.: Closing the loop – Approaches to monitoring the state of the Arctic Mediterranean during the International Polar Year 2007–2008, Progress in Oceanography, 90, 62–89, https://doi.org/https://doi.org/10.1016/j.pocean.2011.02.010, arctic Marine Ecosystems in an Era of Rapid Climate Change, 2011.

Mayer, C.: Large ice loss variability at Nioghalvfjerdsfjorden Glacier, Northeast-Greenland, Nt. Comm., 9, 2768, 2018.

Millgate, T., Holland, P. R., Jenkins, A., and Johnson, H. L.: The effect of basal channels on oceanic ice-shelf melting, Journal of Geophysical Research: Oceans, 118, 6951–6964, 2013.

Münchow, A., Falkner, K. K., Melling, H., Rabe, B., and Johnson, H.: Ocean warming of Nares Strait bottom waters off Northwest Greenland, Oceanography, 24(3), 114–123, https://doi.org/10.5670/oceanog.2011.62, 2011.

Nowicki, S. and Seroussi, H.: Projections of future sea level contributions from the greenland and antarctic ice sheets: Challenges beyond dynamical ice sheet modeling, Oceanography, 31, 109–117, https://doi.org/10.5670/oceanog.2018.216, 2018.

Pelle, T., Morlighem, M., and Bondzio, J. H.: Brief communication: PICOP, a new ocean melt parameterization under ice shelves combining PICO and a plume model, The Cryosphere, 13, 1043–1049, https://doi.org/10.5194/tc-13-1043-2019, 2019.

Rahmstorf, S., Box, J. E., Feulner, G., Mann, M. E., Robinson, A., Rutherford, S., and Schaffernicht, E. J.: Exceptional twentieth-century slowdown in Atlantic Ocean overturning circulation, Nature Climate Change, 5, 475–480, https://doi.org/10.1038/NCLIMATE2554, 2015.

Reese, R., Albrecht, T., Mengel, M., Asay-Davis, X., and Winkelmann, R.: Antarctic sub-shelf melt rates via PICO, Cryosphere, 12, 1969–1985, https://doi.org/10.5194/tc-12-1969-2018, 2018.

Rhein, M., Steinfeldt, R., Huhn, O., Sültenfuß, J., and Breckenfelder, T.: Greenland Submarine Melt Water Observed in the Labrador and Irminger Sea, Geophysical Research Letters, 45, 10,570–10,578, https://doi.org/10.1029/2018GL079110, 2018.

Rietbroek, R., Brunnabend, S.-E., Kusche, J., Schröter, J., and Dahle, C.: Revisiting the contemporary sea-level budget on global and regional scales, Proceedings of the National Academy of Sciences, 113, 1504–1509, https://doi.org/10.1073/pnas.1519132113, 2016.

Rignot, E., Koppes, M., and Velicogna, I.: Rapid submarine melting of the calving faces of West Greenland glaciers, Nature Geoscience, 3, 187–191, https://doi.org/10.1038/NGEO765, 2010.

Rignot, E., Fenty, I., Menemenlis, D., and Xu, Y.: Spreading of warm ocean waters around Greenland as a possible cause for glacier acceleration, Annals of Glaciolog., 53, 257–266, 2012.

Rudels, B., Kohonen, M., Schauer, U., Pisarev, S., Rabe, B., and Wisotzki, A.: Circulation and transformation of Atlantic Water in the Eurasian Basin and the contribution of the Fram Strait inflow branch to the Arctic Ocean heat budget, Progress in Oceanography, 132, 128–152, 2015.

Schaffer, J., von Appen, W.-J., Dodd, P. A., Hofstede, C., Mayer, C., de Steur, L., and Kanzow, T.: Warm water pathways toward Nioghalvfjerdsfjorden Glacier, Northeast Greenland, Journal of Geophysical Research: Oceans, 122, 4004–4020, https://doi.org/10.1002/2016JC012462, 2017.

Schaffer, J., Kanzow, T., von Appen, W. J., von Albedyll, L., Arndt, J. E., and Roberts, D. H.: Bathymetry constrains ocean heat supply to Greenland's largest glacier tongue, Nature Geoscience, 13, 227–231, https://doi.org/10.1038/s41561-019-0529-x, 2020.

Sciascia, R., Straneo, F., Cenedese, C., and Heimbach, P.: Seasonal variability of submarine melt rate and circulation in an East Greenland fjord, Journal of Geophysical Research: Oceans, 118, 2492–2506, https://doi.org/10.1002/jgrc.20142, 2013.

Sciascia, R., Cenedese, C., Nicolì, D., Heimbach, P., and Straneo, F.: Impact of periodic intermediary flows on submarine melting of a Greenland glacier, Journal of Geophysical Research: Oceans, 119, 7078–7098, https://doi.org/10.1002/2014JC009953, 2014.

Seale, A., Christoffersen, P., Mugford, R. I., and O'Leary, M.: Ocean forcing of the Greenland Ice Sheet: Calving fronts and patterns of retreat identified by automatic satellite monitoring of eastern outlet glaciers, Journal of Geophysical Research: Earth Surface, 116, https://doi.org/10.1029/2010JF001847, 2011.

Sheperd, A. and Nowicki, S.: Improvements in ice-sheet sea-level projections, Nature Climate Change, 7, 672–674, https://doi.org/https://doi.org/10.1038/nclimate3400, 2017.

Slater, D. A. and Straneo, F.: Submarine melting of glaciers in Greenland amplified by atmospheric warming, Nature Geosci., 15, 794–799, https://doi.org/https://doi.org/10.1038/s41561-022-01035-9, 2022.

Slater, D. A., Goldberg, D. N., Nienow, P. W., and Cowton, T. R.: Scalings for submarine melting at tidewater glaciers from buoyant plume theory, Journal of Physical Oceanography, 46, 1839–1855, https://doi.org/10.1175/JPO-D-15-0132.1, 2016.

Slater, D. A., Carroll, D., Oliver, H., Hopwood, M. J., Straneo, F., Wood, M., Willis, J. K., and Morlighem, M.: Characteristic Depths, Fluxes, and Timescales for Greenland's Tidewater Glacier Fjords From Subglacial Discharge-Driven Upwelling During Summer, Geophysical Research Letters, 49, 794–799, https://doi.org/10.1029/2021GL097081, 2022.

Smith, B., Fricker, H. A., Gardner, A. S., Medley, B., Nilsson, J., Paolo, F. S., Holschuh, N., Adusumilli, S., Brunt, K., Csatho, B., Harbeck, K., Markus, T., Neumann, T., Siegfried, M. R., and Zwally, H. J.: Pervasive ice sheet mass loss reflects competing ocean and atmosphere processes, Science, 368, 1239–1242, https://doi.org/10.1126/science.aaz5845, 2020.

Storch, H. v. and Zwiers, F. W.: Statistical Analysis in Climate Research, Cambridge University Press, https://doi.org/10.1017/CBO9780511612336, 1984.

Straneo, F. and Cenedese, C.: The Dynamics of Greenland's Glacial Fjords and Their Role in Climate, Annual Review of Marine Science, 7, 89–112, https://doi.org/10.1146/annurev-marine-010213-135133, 2015.

Straneo, F. and Heimbach, P.: North Atlantic warming and the retreat of Greenland's outlet glaciers, Nature, 504, 36–43, https://doi.org/https://doi.org/10.1038/nature12854, 2013.

Straneo, F., Sutherland, D. A., Holland, D., Gladish, C., Hamilton, G. S., Johnson, H. L., Rignot, E., Xu, Y., and Koppes, M.: Characteristics of ocean waters reaching Greenland's glaciers, Annals of Glaciology, 53, 202–210, https://doi.org/10.3189/2012AoG60A059, 2012.

Swingedouw, D., Houssais, M.-N., Herbaut, C., Blaizot, A.-C., Devilliers, M., and Deshayes, J.: AMOC Recent and Future Trends: A Crucial Role for Oceanic Resolution and Greenland Melting?, Frontiers in Climate, 4, https://doi.org/10.3389/fclim.2022.838310, 2022.

Wang, Q., Wekerle, C., Wang, X., Danilov, S., Koldunov, N., Sein, D., Sidorenko, D., von Appen, W.-J., and Jung, T.: Intensification of the Atlantic Water Supply to the Arctic Ocean Through Fram Strait Induced by Arctic Sea Ice Decline, Geophysical Research Letters, 47, e2019GL086 682, https://doi.org/https://doi.org/10.1029/2019GL086682, 2020.

Wilson, N., Straneo, F., and Heimbach, P.: Satellite-derived submarine melt rates and mass balance (2011–2015) for Greenland's largest remaining ice tongues, The Cryosphere, 11, 2773–2782, https://doi.org/10.5194/tc-11-2773-2017, 2017.

Wilson, N. J. and F. Straneo, F.: Water exchange between the continental shelf and the cavity beneath Nioghalvfjerdsbrea (79 North Glacier), Geophysical Research Letters, 42, 7648–7654, 2015.

Wood, M., Rignot, E., Fenty, I., An, L., Bjørk, A., van den Broeke, M., Cai, C., Kane, E., Menemenlis, D., Millan, R., Morlighem, M., Mouginot, J., Noël, B., Scheuchl, B., Velicogna, I., Willis, J. K., and Zhang, H.: Ocean forcing drives glacier retreat in Greenland, Science Advances, 7, 1–11, https://doi.org/10.1126/sciadv.aba7282, 2021.

Xu, Y., Rignot, E., Menemenlis, D., and Koppes, M.: Numerical experiments on subaqueous melting of greenland tidewater glaciers in response to ocean warming and enhanced subglacial discharge, Annals of Glaciology, 53, 229–234, https://doi.org/10.3189/2012AoG60A139, 2012.

Yin, Z.: Ice-ocean interactions in a Greenland fjord, Master's thesis, Department of Meteorology, Stockholm University, Sweden, 2020.